Graduate Theses and Dissertations   Graduate School

November 2017

DNS and LES of Scalar Transfer Across an Air-water Interface during Inception and Growth of Langmuir Circulation

Amine Hafsi
University of South Florida, ahafsi@mail.usf.edu

Follow this and additional works at: https://scholarcommons.usf.edu/etd

Part of the Civil Engineering Commons, and the Ocean Engineering Commons

DNS and LES of Scalar Transfer Across an Air-water Interface during Inception and Growth of

Langmuir Circulation

by

Amine Hafsi

A dissertation submitted in partial fulfillment
of the requirements for the degree of
Doctor of Philosophy
Department of Civil and Environmental Engineering
College of Engineering
University of South Florida

Major Professor: Andrés E. Tejada-Martínez, Ph.D.
Rasim Guldiken, Ph.D.
Fabrice Veron, Ph.D.
Mark Ross, Ph.D.
Ping Wang, Ph.D.

Date of Approval:
November 13, 2017

Keywords: Small scale Langmuir cell, Stokes drift velocity, Direct numerical
simulation

DEDICATION

This dissertation is dedicated to my parents Fethia and Mohamed, my wife Jeanie and my siblings who were my inspiration and motivation throughout my PhD journey and without them this achievement would not have been possible. I also dedicate this work to my two beautiful kids Jennah and Adam who have been the reason for my hard work and motivation and the driving force that pushed me to overachieve, wishing that my accomplishment make them proud.

ACKNOWLEDGMENTS

I would like to express my sincere gratitude and acknowledgement of my advisor, Dr. Andrés E. Tejada-Martínez, for his help, support and guidance throughout my PhD journey. I would like to sincerely thank him for the opportunity he gave me to contribute towards the understanding of this research. Our many conversations helped in guiding this research in the right direction. I would also like to give a special thank you to my wife, Jeanie, for her patience, help and unconditional support. Thanks for sticking with me through all the ups and downs of this lengthy journey. Without you Jeanie, I would have never achieved the goals of this research. Also, to both of my children Jennah and Adam, who reminded me daily why it is possible to set up goals in life and achieve them no matter how hard they appear. Finally, to my parents, Fethia and Mohamed, and to my siblings, thank you all for your endless support and love.

A special and sincere thank you goes to Prof. Fabrice Veron for our conversations which guided me in many occasions towards finding solutions to challenges I had faced throughout my research.

I am also grateful to my other committee members Dr. Rasim Guldiken, Prof. Mark Ross and Prof. Ping Wang for their time, effort and for their valuable feedback. Additional thanks go to my committee chairperson, Prof. Mohamed Elhamdadi for his time and effort at my doctoral dissertation defense.

It was also my great pleasure to be part of an amazing Computational Environmental Fluid Mechanics team at USF of wonderful and bright intellectuals with whom I shared doctoral studies

with, I would mention a few of them here, Dr. Nityanand Sinha with whom I had the pleasure to discuss the progress of my research with in many occasions, Dr. Roozbeh Golshan for his support and kindness, and my graduate colleagues, to mention a few, Keisha Pierre, and my good friends Ali Aldrees and Dr. Abdulrahman Al Fuhaid.

Finally, I would like to also acknowledge the support from the Sloan Foundation, the National Science Foundation and the University of South Florida for their fellowships which allowed me to achieve the goals of my doctorate.

TABLE OF CONTENTS

LIST OF FIGURES

iv

ABSTRACT

Direct numerical simulations (DNS) of an initially quiescent coupled air-water interface driven by an air flow with free stream speed of 5 m/s have been conducted. The DNS solves a scalar advection-diffusion equation for dissolved gas (or scalar) concentration in order to determine the impact of the water-side turbulence on scalar (mass) transfer from the air side to the water side and subsequent vertical transport in the water column. Two simulations are compared: one with a freely deforming interface and a second one with a flat interface. In the first simulation, the deforming interface evolves in the form of gravity-capillary waves generating aqueous Langmuir turbulence characterized by small-scale (centimeter-scale) Langmuir cells (LCs). The second simulation is characterized by pure shear-driven turbulence in the absence of LCs as the interface is intentionally held flat. It is concluded that the Langmuir turbulence serves to enhance vertical transport of the scalar in the water side and in the process increases scalar transfer efficiency relative to the shear-dominated turbulence in the flat interface case. Furthermore, transition to Langmuir turbulence was observed to be accompanied by a spike in scalar flux via molecular diffusion across the interface characterized by an order of magnitude increase. Such episodic flux increases, if linked to gusts and overall unsteadiness in the wind field, are expected to be an important contributor in determining the long-term average of the air-sea gas fluxes. The effectiveness of popular transfer velocity models, namely the small eddy model and the surface divergence model, in predicting this spike is evaluated via the DNS. In addition to LCs,

DNS reveals that the water side turbulence is characterized by smaller, shear-driven turbulent eddies at the surface embedded within the LCs. LES with momentum equation augmented with the well-known Craik-Leibovich (C-L) vortex force is used to understand the roles of the wave and shear-driven LCs (i.e. the Langmuir turbulence) and the smaller shear-driven eddies (i.e. the shear turbulence) in determining molecular diffusive scalar flux from the air side to the water side and vertical scalar transport beneath. The C-L force consists of the cross product between the Stokes drift velocity (induced by the interfacial waves) and the flow vorticity. It is observed that Stokes drift shear intensifies the smaller eddies (with respect to purely wind-driven flow, i.e. without wave effects) leading to enhanced diffusive scalar flux at the air-water interface. LC leads to increased vertical scalar transport at depths below the interface and thus greater scalar transfer efficiency.

CHAPTER 1: INTRODUCTION

1.1. Context

In the last few decades, our planet has been undergoing drastic changes to its carbon cycle which is the main cause of global warming. This is attributed to the dramatic increase of greenhouse gases such as carbon dioxide (CO_2) in the atmosphere due to the increasing industrialization of our societies. Greenhouse gases absorb solar energy and release it into the atmosphere, a process that keeps our planet warmer than it would be without the presence of these gases. A significant portion of these greenhouse gases interacts with the oceans because of the fact that oceans take up more than 70 % (the majority) of the surface of the earth in total. The United States Environmental Protection Agency (EPA) suggests that CO_2 represents the majority (84%) of all greenhouse gases generated by human activities. Furthermore, about 30% to 40% of anthropogenic CO_2 is taken up by the oceans (Donelan and Wanninkhof, 2002). The accuracy of this latter assumption is arguable however given how difficult it is to predict and field-measure gas (mass) transfer rates across wind-driven air-sea interfaces due to the infinitesimal sizes of adjacent molecular sublayers below and above the interface.

Gas (or scalar) flux across the air-water interface can be expressed as the product of concentration difference across the interface and transfer velocity. The latter is a measure of transfer efficiency which for sparingly soluble gases such as CO_2 depends on turbulence characteristics within the boundary layer of the water side in particular. This is due to the fact that for sparingly soluble gases, their diffusivity in water is three to four times order of magnitudes

1

lower than their diffusivity in air. Consequently, oceanic turbulence structure and boundary layer dynamics in the vicinity of few millimeters immediately below the air-water interface greatly influence gas transfer rates (Figure 1.1).
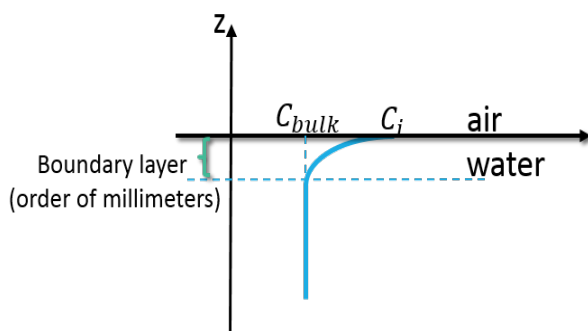
Figure 1.1 Molecular diffusive boundary layer in terms of dissolved gas (scalar) concentration in the water side. C_i is the concentration at the air-water interface and C_{bulk} is the concentration in the bulk of the water column.

The available gas transfer models or parameterizations as of today, which attempt to predict gas uptakes in oceans, have shown limitations by resulting in predictions not agreeing with each other. For example, if the methods of Liss and Merlivat (1986) and Wanninkhof and McGillis (1999) were to be used to estimate CO_2 uptake in oceans, these methods would result in uptakes of approximately 1.1 PgC /year and 3.3 PgC/year respectively (Banerjee and MacIntyre, 2007). This variation of a factor of three between these methods is large enough to suggest these methods are not reliable in accurately predicting gas uptakes and thus there is a pressing need for more reliable methodologies to estimate gas transfer in oceans. Furthermore, for gas transfer models or parameterizations to be accurate they must include a good representation of the turbulence characteristics of the boundary layer that are not yet well understood.

Near-surface aqueous turbulence and boundary layer characteristics depend on various mechanisms such as wave-breaking, wind shear, stratification and surface heat fluxes. The major processes controlling gas transfer through the wind-induced air-sea interface are turbulent-induced diffusive transport exchange as well as exchange driven by bubbles generated from the breaking of ocean waves (Frew et al., 2004). At high wind speeds (greater than 8 m s^{-1}), the air-sea interface (wave) breaking intensifies thereby generating droplets that disperse in the air and bubbles that are engulfed into the water side (Zhao, 2006). At low and moderate wind speeds (less than 3 m s^{-1}), the shear stress acting on the air-sea interface generates turbulent eddies on the water side which are the main controlling factors of transfer of sparingly soluble gases across the interface via diffusion (Komori, 1993).

Gas transfer velocity determines how fast the gas uptake through the air-water interface occurs making it the physical factor to parametrize. Wind speed models are frequently used to predict gas transfer velocity into the water surface for different turbulent mixing conditions. One of the popular models is the Wanninkhof (1992) model which directly links the transfer velocity to the speed of wind at a height of 10 m above the air-water interface u_{10}:

$$k_L = 0.31 * u_{10} \tag{1.1}$$

Wanninkhof and McGillis (1999), determined another relationship between gas transfer velocity and u_{10}, this time as a cubical correlation:

$$k_L = 0.028 * u_{10}{}^3 \tag{1.2}$$

3

Wanninkhof (1992) however concluded that "*Many uncertainties regarding the relationship between gas transfer and wind speed remain. It is not clear whether wind speed can be used by itself to estimate gas transfer velocities.*" Indeed, estimating gas transfer using u_{10} or even using free-stream wind speed (Wanninkhof et. al, 2009) can be uncertain because all these models have a poor level of accuracy or they were established using laboratory data within conditions that are certainly not reflective of field conditions, while the models established using field data relied on data that is not necessarily accurate or validated.

An alternative to wind speed-based parameterizations, surface renewal theory is one of the widely accepted theories used to obtain parameterizations of gas transfer velocity. Surface renewal theory is based on the principle that turbulent eddies bring up low concentration fluid packages from below intermittently. According to surface renewal theory, transfer velocity can be obtained as

$$k_L = (D/\tau)^{1/2} \tag{1.3}$$

where τ is the surface renewal time scale of the turbulent eddies and D is the molecular diffusivity in water.

In this dissertation, it should be noted that diffusivity and boundary layer turbulence are the prevailing factors driving the sparingly soluble gas transfer across the air-water interface (absent wave-breaking) whereas the chemistry effects are secondary and consequently not considered. Indeed, Doney (2006), for his "Gas exchange across the air-sea interface" lecture for a Marine Chemistry course given at Massachusetts Institute of Technology wrote in notes made available to the class the following: "*It is possible to assess the significance of this by comparing*

the time constant of this buffering reaction, which is of the order of a minute, with the time it takes

for a molecule to transit the boundary layer via molecular diffusion, which is related to:

$T \approx \frac{L^2}{D}$ *and using typical values* $L = 40 \times 10^{-6} m^2$ *and* $D = 2 \times 10^{-9} m^2 s^{-1}$ *which substituted*

in the above yields $T \approx 1s$. *Thus a CO2 molecule spends far too little time in the boundary layer*

to be affected by chemical reaction whilst there".

Doney (2006) also suggests that films present at the air-sea interface may contain catalysts such as carbonic anhydrase that could potentially speed up the chemical reaction of CO2. Nevertheless, he reveals that measurements of bulk seawater do not show carbonic anhydrase concentrations in sufficient quantity for any catalyzation to happen. Because of the earlier arguments, it is believed that chemical reaction of anthropogenic gases while entering the air-sea interface is not of any significance compared to the complex physical mechanisms which take place within the microscopic boundary layer of both sides of the air-sea interface.

1.2. Motivation and Objectives

At the air-sea interface, wave-current interaction, during low winds speeds on the order of 1-2 m s^{-1}, leads to the generation of small (centimeter-scale) eddies known as Langmuir cells (LC) consisting of counter-rotating vortices parallel to the direction of the wind (see sketch in Figure 1.2a). The manifestation of these vortices on the water side at the air-water interface was observed experimentally by Veron and Melville (2001) in terms of temperature as seen in Figure 1.2b. For example, here the blue streaks correspond to the surface convergences of the LC.

The measurements of Veron and Melville (2001) showed that the inception of small scale LC and subsequent transition to Langmuir turbulence (prior to the onset of micro-breaking wind

waves[1]) leads to a 70% increase in gas or mass transfer velocity, demonstrating the strong impact of LC on gas transfer across the air-water interface. Transition to Langmuir turbulence refers to when the initially coherent vortices become unstable and loose coherency as they start to interact with each other nonlinearly. The measurements of Veron and Melville (2001) were collected under a gradually increasing wind with final speed of 5 m/s at a fetch of 10.72 m and during the presence of gravity-capillary waves possessing wavelengths up to 10-15 cm.

(a)   (b)
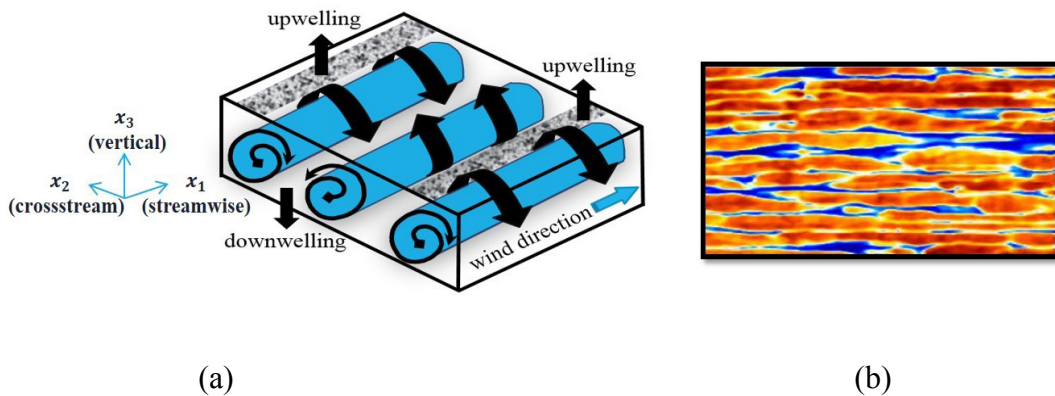
Figure 1.2 (a) Sketch of centimeter-scale Langmuir cells aligned in the direction of the wind and (b) surface temperature image (red is warmer) in wind-driven air-water interface in laboratory measurements of Veron and Melville (2001) during the presence of small-scale Langmuir cells. Langmuir cells are generated by wave-current interaction.
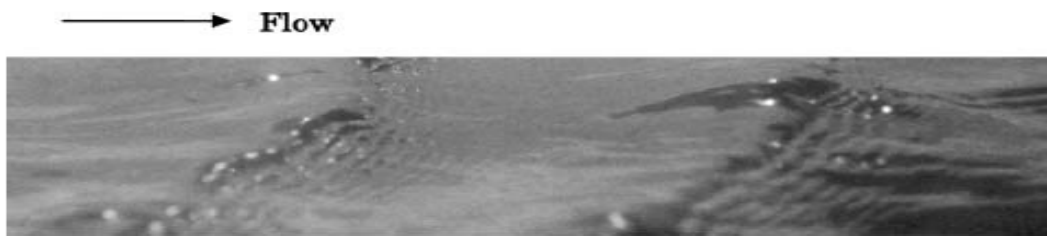
Figure 1.3 Photograph showing complex structure of short gravity-capillary wave field associated with micro-breaking in wave-tank experiment (from Komori et al., 2010).

---

[1] Micro-breaking wind waves refers to the breaking of gravity capillary waves without significant air entrainment.

Komori et al. (2010) performed a direct numerical simulation (DNS) similar to the laboratory setting of Veron and Melville (2001). In their DNS, LC-like structures coexisting with micro-breaking capillary waves riding on larger gravity-capillary waves were identified (similar to those in Figure 1.3). However, only recently researchers have begun using DNS to investigate LC-like structures and their connection with gas transfer across the air-water interface such as Takagaki et al.'s work in 2015.

Because of the complexity of successfully running a DNS, early DNS, conducted to study mass transfer across the air-sea interface and analyse the characteristics of interfacial turbulence signatures, used either flat interfaces (e.g. Nagaosa et al., 2012) or weakly deforming interfaces (Hung and Tsai, 2007). Neither of these approaches is able to capture the wave-current interaction mechanism generating LC. Also, in most cases these simulations did not resolve the air side. In the more recent DNS of Tsai et al. (2013), while they were able to simulate the turbulent structure below capillary waves and its impact on mass transfer, their simulation started from an imposed wave field, thus bypassing the wave generation by winds. This would not allow the investigation of the dependence of the turbulence on wind speed, which is typically a key component of parameterizations of transfer velocity. Furthermore, the simulation of Tsai et al. (2013) did not resolve the air-side and consequently they noted that the coupling between the air and water phases and the natural randomness of such a two-phase flow is missing in their methodology. Thus they recommended the use of more realistic methodologies for the study of air-sea interfacial mass transfer. Tsai et al. (2013) have said the following in particular: "The posed canonical problem in the present numerical simulation is an idealized model of wind-driven surface waves and turbulent flow. It neglects the coupling between the air and water flows, and also the ambient randomness

and three-dimensionality of the natural forcing and thus is certainly a simplification of the settings in the wind-wave flume and the real oceans. "

The DNS of Komori et al. (2010) was performed with a multi-phase code and thus resolved both air and water sides enabling them to capture complex deforming gravity waves with micro-breaking ripples representative of reality. Nevertheless, as mentioned earlier, their study did not analyse the effects of aqueous turbulence on mass transfer across the air-sea interface.

To attain the objectives of this study it is essential to perform a three-dimensional multiphase DNS of a wind-driven coupled air-water interface. These computations are made to better understand the impact of small-scale LC on interfacial air-sea mass transfer. First, a DNS is developed of a coupled air-water interfacial flow with a wind speed similar to the wind speed considered by Veron and Melville (2001) and Komori et al. (2010), to capture the deforming air-water interface characterized by micro-breaking capillary waves along with the induced turbulence signatures just beneath the air-sea interface. This methodology will be validated numerically via comparison with the DNS of Komori et al. (2010).

In the experiments of Veron and Melville (2001), initiation of laminar LCs was followed by a sudden transition to Langmuir turbulence in which the growing LCs were characterized by irregularity while nonlinearly interacting with each other. In these physical experiments, the transition to Langmuir turbulence was accompanied by a spike in molecular diffusive scalar (gas) flux from the air to the water side, suggesting strong dependence of the flux on the waves and LC. One of the main objectives of this study is to further establish this process numerically while highlighting the importance of LC in determining the vertical transport of the scalar. As such, it is hypothesized that mass or scalar transfer efficiency measured in terms of transfer velocity is

enhanced in the presence of LCs which should provide intense surface renewal. This will be possible to observe by comparing results from two DNS simulations, one simulation with a freely deforming interface (giving rise to gravity-capillary waves generating aqueous Langmuir turbulence characterized by small-scale (centimeter-scale) Langmuir cells (LCs)) and the other with the interface intentionally held flat (i.e. without LCs). This will be the subject of Chapter 4.

Additionally the results from the DNS will be used to test the accuracy of parameterization models of mass transfer velocity based on surface renewal theory such as the small eddy model of Zappa et al. (2007) and the surface divergence model (Banerjee, 2007). This will also be evaluated in Chapter 4. Note that these models provide physically-grounded alternatives to the widely used models obtained from empirical relationships purely based on wind speed which disregard important physical processes such as LC which should play important roles in determining mass transfer velocity.

Lastly, Takagaki et al. (2015), in a DNS configuration similar to that of Komori et al. (2010) and the present DNS, performed a scale separation of the aqueous turbulence into the wave and wind shear-generated LCs and the smaller scale, less coherent turbulence. Takagaki et al. (2015) concluded that the smaller scale turbulence (characterized by eddies of sizes smaller than LCs) and not the LCs are responsible for determining the scalar or mass transfer across the air-water interface via molecular diffusion. Nevertheless, the role of the waves and associated LCs in determining molecular diffusive scalar flux should be further investigated/clarified in light of the physical experiments of Veron and Melville (2001) which showed that generation of LCs and associated transition to Langmuir turbulence leads to a spike in gas (mass) transfer velocity. In Chapter 5 we will investigate the role of the waves and LCs and their interaction with the smaller

scale turbulence in determining molecular diffusive scalar flux across the air-water interface and the turbulent vertical flux of scalar throughout the water column. This investigation will be performed via large-eddy simulation (LES) based on the well-known Craik-Leibovich (CL) vortex force (Craik and Leibovich, 1976) which augments the momentum equations and parameterizes the wave-current interaction generating the LC without the need to resolve the gravity-capillary waves at the interface. The C-L vortex force allows imposition of the Stokes drift induced by the waves and thus a convenient platform (unlike DNS) for understanding the effect of the waves through the Stokes drift shear on the turbulent scales, in particular the LCs and the smaller eddies at the surface, and ultimately the scalar (mass) transfer across the air-water interface via molecular diffusion and vertical scalar transport by the aqueous eddies.

1.3. Organization of the Dissertation

This dissertation is organized as follows. Chapter 2 presents a literature review about turbulence from its physical aspect and its mathematical aspect followed by a discussion about the simulation methodologies and computational tool used in this study. In Chapter 3 a description of the boundary layer exchange at the air-water interface and current transfer velocity parametrizations is presented. In Chapter 4 the adopted DNS computational methodology will be explained in great details and its results analysed with an emphasis on the Langmuir turbulence structure resolved and its impact on vertical transport of the scalar on the water side. The second part of Chapter 4 in particular presents transfer velocity results from surface renewal parameterizations (i.e., the small eddy model and the surface divergence model) using the DNS data and assesses these parameterizations via comparison with the transfer velocity measured directly in the DNS. Following that, in Chapter 5 the role of the waves and associated LCs in determining molecular diffusive scalar flux of scalar at the air-water interface will be explained

through LES. Finally, Chapter 6 summarizes the conclusions of this research in addition to providing recommendations for future work.

CHAPTER 2: COMPUTATIONAL APPROACHES TO TURBULENCE AND NUMERICAL METHOD

The main purpose of this dissertation is to numerically study scalar (mass) transfer across a wind-driven air-water interface characterized by non-breaking gravity-capillary waves and grasp the physical turbulent mechanisms controlling it. This knowledge should allow for future improved parametrization of mass transfer through the air-water interface. This chapter first includes a review of turbulence in terms of its physical properties followed by an introduction to the available numerical approaches suitable to solving the turbulent flow associated with a wind-driven air-water interface.

2.1. What is Turbulence?

When a liquid or a gas substance flows irregularly and develops random chaotic vortices in the three-dimensional directions, it is likely that the flow may be considered turbulent. Turbulent motions are characterized by the coexistence of a wide range of scales from small-scale eddies and bulges to as large as potentially the fluid domain. Turbulence is the most common state of fluid motion occurring in nature. For example, fluid flowing in a state of turbulence can be easily recognizable in river flows and waterfalls or even felt on an airplane when it cuts through mixing areas between jet streams with different air speeds. Many more examples of turbulence occurring in nature present challenges the majority of engineering and scientific disciplines are dealing with, which include but not limited to aeronautics, nuclear engineering and applied sciences such as oceanography, meteorology, and environmental sciences.

2.2. The Physical Features of Turbulence

Although it is difficult to precisely define turbulence, scientists certainly would agree on a number of characteristics of turbulence listed below:

- Turbulent flows are irregular.

- Turbulent flows are rotational and three-dimensional.

- Turbulent flows are both diffusive and dissipative.

- Turbulent flows occur at high Reynolds numbers.

- Turbulent flows are characterized by a wide range of spatial and temporal scales.

- Turbulent flows are continuum phenomena.

2.3. Governing Equations

The equations describing the motions of any Newtonian, incompressible fluid flow are the continuity equation (2.1), and the Navier-Stokes equations (2.2). Using the Einstein indicial notation, the dimensionless governing equations are:

$$\frac{\partial u_i}{\partial x_i} = 0 \tag{2.1}$$

$$\frac{\partial u_i}{\partial t} + u_j \frac{\partial u_i}{\partial x_j} = -\frac{\partial p}{\partial x_i} + \frac{\partial \tau_{ij}^v}{\partial x_j} \tag{2.2}$$

where u_i denotes the velocity field ($i = 1, 2$ and 3 respectively represent the streamwise (or downwind), spanwise and vertical directions), p is the pressure field divided by density and τ_{ij}^v is the molecular viscous stress defined as:

13

$$\tau_{ij}^v = \frac{1}{R_e}\left(\frac{\partial u_i}{\partial x_j} + \frac{\partial u_j}{\partial x_i}\right) \tag{2.3}$$

where $R_e = U_0 D / \nu$ is the Reynolds number, defined as a ratio of inertial forces to viscous forces, which quantifies the importance of advection relative to diffusion. Furthermore, U_0 is a characteristic velocity of the flow, D is a characteristic dimension and ν is the kinematic viscosity of the fluid.

Using (2.1), (2.2) can be re-expressed as

$$\frac{\partial u_i}{\partial t} + u_j \frac{\partial u_i}{\partial x_j} = -\frac{\partial p}{\partial x_i} + \frac{1}{Re}\frac{\partial^2 u_i}{\partial x_j^2} \tag{2.4}$$

In addition to the continuity and momentum (Navier-Stokes) equations to predict air and water flow velocities and pressures, we will also consider concentration of a dissolved scalar (i.e. gas) in air and in water as predicted via a scalar transport equation:

$$\frac{\partial C}{\partial t} + u_j \frac{\partial C}{\partial x_j} = \frac{1}{R_e S_C}\frac{\partial^2 C}{\partial x_j \partial x_j} \tag{2.5}$$

where S_C is the Schmidt number defined as kinematic viscosity divided by scalar diffusivity. For example, for CO_2 dissolved in water the Schmidt number is ~200, implying that the diffusive molecular boundary layer is much smaller than the viscous momentum boundary layer. In this study, as has been done in others, the Schmidt number is set to 1 because this does not affect the

fundamental turbulent mechanisms promoting mass (scalar) transfer across the interface. A Schmidt number of 200 would require a more expensive computation in order to resolve the thinner diffusive boundary layer.

2.4. Numerical Approach to Turbulence Simulation

2.4.1. Direct Numerical Simulation (DNS)

DNS is the most reliable approach to solve the full instantaneous Navier-Stokes equations because it is the only approach that resolves all the spatial scales from the smallest dissipative scales of turbulence through the largest scales of turbulence. This means that the numerical simulation will have to employ a dense enough computational meshing scheme that is capable of resolving all the dynamics involved with the smallest eddies of the flow as a well as a sufficiently large domain to capture the largest of the scales. As per Kolmogorov theory (Pope, 2000), the number of grid points suggested for a three-dimensional DNS simulation needs to be $N \sim R_e^{9/4}$, where Re is the Reynolds number defined earlier. The range of scales in turbulent flows increases with increasing Reynolds number, and in cases where Reynolds numbers are exceedingly high, the use of DNS can be a challenge. For these reasons the flows suitable for a DNS would be those with low to moderate Reynolds numbers.

DNS provides the advantage of solving the governing equations directly, which allows accurate resolution of all spatial scales of turbulence without the need or use of a turbulence model or parameterization. Another advantage of DNS is the opportunity it gives to examine flow characteristics that can be difficult to measure via physical experiments such as pressure-strain correlations (Pope, 2000). Though, one of its disadvantages is the fine grid needed to allow all the smallest features of turbulence to be resolved which drives the cost of the computation to be high.

However, with the rapid improvement of high performance supercomputers in the last decade, it is nowadays possible to overcome the astronomical amount of computation needed for DNS of certain flows.

2.4.2. Large Eddy Simulation (LES)

LES is an alternative methodology to DNS which focuses on separating scales of large energy-containing eddies and small energy-dissipating eddies. The small scales can be too computationally expensive to simulate. Therefore, rather than including all the small scales in the computation, LES uses a low-pass filtering operation to pass the large scales up to a chosen filter width Δ and damp (or filter out) the smaller scales (see Figure 2-1).
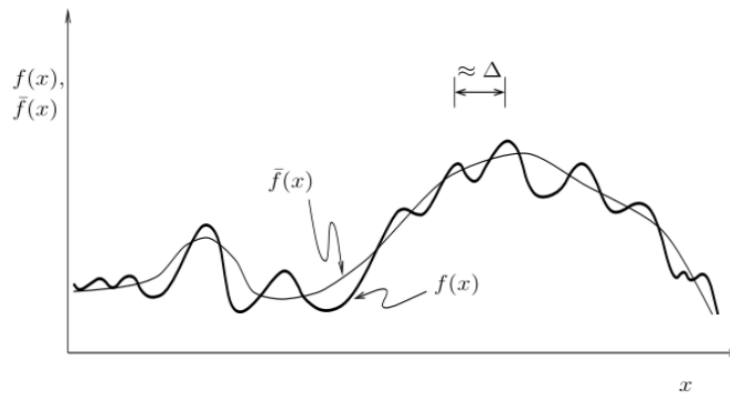
Figure 2.1 Sketch of functions $f(x)$ and filtered function $\bar{f}(x)$ with spatial filter of width Δ (Tejada-Martínez, 2002).

This filtering operation is applied to the Navier-Stokes equations generating a subgrid scale (SGS) stress in these equations which indirectly accounts for the effect of motions of the unresolved or damped scales. Solution of the filtered Navier-Stokes equations yields the filtered flow variables describing the behavior of the larger, energy-containing eddies. The SGS stress

16

appearing in the filtered Navier-Stokes equations presents a closure problem requiring approximation of the effect of the unresolved scales on the resolved ones in terms of resolved quantities.

The filtered governing equations in an LES are as follows:

$$\frac{\partial \bar{u}_i}{\partial x_i} = 0 \tag{2.6}$$

$$\frac{\partial \bar{u}_i}{\partial t} + \bar{u}_j \frac{\partial \bar{u}_i}{\partial x_j} = -\frac{\partial \bar{p}}{\partial x_i} + \frac{1}{R_e}\frac{\partial^2 \bar{u}_i}{\partial x_j \partial x_j} + \frac{\partial \tau_{ij}^{SGS}}{\partial x_j} \tag{2.7}$$

where the over-bar denotes application of the filter and thus $\bar{u}_i$ is the i-th component of the space-filtered (resolved) velocity field while $\bar{p}$ is the space-filtered (resolved) pressure field. The SGS stress tensor τ_{ij}^{SGS} , which appears in filtered momentum equation, accounts for the effect of the filtered-out (unresolved) scales on the resolved scales and is defined as follows:

$$\tau_{ij}^{SGS} = \bar{u}_i \bar{u}_j - \overline{u_i u_j} \tag{2.8}$$

Since the unfiltered velocity u_i is not resolved within the LES approach, the SGS stress presents a closure problem. For this reason, this stress must be modeled in terms of resolved quantities. The interested reader is directed to Pope (2000) for description of popular SGS stress models.

2.4.3. Reynolds Averaged Navier-Stokes (RANS)

Simulation based on the RANS equations (i.e. RANS simulation) is the most affordable methodology to simulate turbulent flows, though it is the least accurate of the three methodologies since it does not attempt to resolve any of the turbulent scales and exclusively focuses on resolving the mean components of the flow. RANS is derived by averaging Navier-Stokes equations over time, resulting either in the set of steady equations for mean quantities in the case of steady RANS or a set of evolution equations for slow varying averaged variables (slower than the turbulence) in the case of unsteady RANS. Similar to LES, the RANS equations possess an unresolved stress, namely the well-known Reynolds stress. Closure of the Reynolds stress is provided by a turbulence model such as the popular k-epsilon model (Pope, 2000). Although RANS is particularly more efficient than LES and DNS, this methodology only computes mean quantities of the flow, hence, it does not capture any of the turbulent scales, a task that is needed in order to better analyze the turbulence behind mass transfer across the air-water interface which is the subject of this dissertation. Thus, DNS and LES are the methodologies to be used in this work.

2.5. Numerical Method and Framework

The flow solver used in this research is based on the open source numerical collection of C++ libraries OpenFOAM (Open source Field Operations and Manipulations) which uses the finite volume method to discretize the continuity, Navier-Stokes and scalar equations, reviewed earlier. After the discretization of the Navier-Stokes equations, the resulting pressure-velocity coupling for the momentum equation is solved using the PIMPLE method which is a combination of the Pressure Implicit with Splitting of Operators (PISO) method (Márquez Damián, 2013) and the Semi-Implicit Method for Pressure-Linked Equations (SIMPLE) method (Patankar, 1972).

InterFOAM, a solver included with OpenFOAM and widely used to simulate two-phase flows, will be employed to compute the wind-driven air-water interfacial turbulent flows of focus in this thesis. InterFOAM tracks the air-water interface via a modified volume of fluid multiphase methodology based on solving an advection transport equation for a volume phase fraction, which was created following a manipulation of the original methodology of Hirt et. al (1981). The next paragraphs will discuss in more details the methodology used by OpenFOAM.

2.5.1. The Finite Volume Method (FVM)

In the finite volume method, a three-dimensional computational domain is subdivided into a finite number of control volumes of any general polyhedral shape with variable numbers of neighboring volumes, hence, allowing any possible meshing scheme (i.e., structured or unstructured). Consequently, the integral form of the governing equations is discretized over the control volumes. Surface and volume integrals are linearized using suitable discretization methods and the solution of the linearized equations is achieved using an iterative linear equation solver (see OpenCFD, 2012 for details on linear equation solvers).

2.5.2. Volume of Fluid Methodology (VoF)

The volume of fluid method is a technique used to track multiphase interfaces. Its concept was first published by Hirt & Nichols (1981), although already established a decade earlier. The VoF method is based on the idea of a volume fraction defined such that it varies between 0 and 1, i.e. it is unity (1 or 100%) if a cell is fully occupied by a fluid of choice (water in the present study) and zero if it is not occupied by the fluid of choice (meaning that it is fully occupied by air in the present study).

OpenFOAM, which uses an improved VoF approach, has gained its popularity from accurately tracking and locating interfaces between different fluids due to the incorporation of an

interfacial compression flux term to mitigate the effects of numerical smearing of the interface

between two liquids (Deshpande et al., 2012) and from its advantage of being fully conservative.

In addition to the continuity and momentum equations, the governing equations of the VoF

methodology include equations which take into consideration multi-phases via a phase fraction

parameter γ which varies between 0 and 1, and physical properties of the fluids, i.e. dynamic

viscosity and density of each phase, as well as the surface tension σ. In this present DNS the

density of water and air were chosen as $1000\ \text{kg/m}^3$ and $1.2048\ \text{kg/m}^3$ respectively, the air

water surface tension was chosen as $0.07286\ \text{N/m}$ and the kinematic viscosity of water and air

were set to $1.0 \times 10^{-6}\ \text{m}^2/\text{s}$ and $1.5 \times 10^{-5}\ \text{m}^2/\text{s}$ respectively. In this study two fluids are

considered (i.e., water and air). Denoting subscript "w" for water and "a" for air, the VoF

methodology is expressed via the following equation for volume phase fraction, γ

$$\frac{\partial \gamma}{\partial t} + \nabla.(\gamma \boldsymbol{U}) + \nabla.[(\boldsymbol{U}_w - \boldsymbol{U}_a)\gamma(1-\gamma)] = 0 \qquad (2.9)$$

Fluid velocity $\boldsymbol{U}$ (u_i), density ρ and viscosity μ are expressed as

$$\boldsymbol{U} = \boldsymbol{U}_w \gamma + \boldsymbol{U}_a(1-\gamma) \qquad (2.10)$$

$$\rho = \rho_w \gamma + \rho_a(1-\gamma) \qquad (2.11)$$

$$\mu = \mu_w \gamma + \mu_a(1-\gamma) \qquad (2.12)$$

20

where $\gamma = 1$ for water (i.e., this value corresponds to a finite volume (or grid) cell with 100% of its volume occupied by water) and $\gamma = 0$ for air (i.e., this value corresponds to a cell with 100% of its volume occupied by air). Thus U_w and U_a are the fluid velocities in water and in air, respectively, ρ_w and ρ_a are densities of water and air, respectively and μ_w and μ_a are dynamic viscosities of water and air, respectively. The above VoF methodology implemented in openFOAM follows the original methodology of Hirt et al. (1981) while incorporating a compression flux term (the 3rd term on the left hand side of equation 2.9) to lessen the effects of numerical smearing of the interface between the two phases (Deshpande et al., 2012) and therefore improve the sharpness of the interface.

2.5.3. Validation of OpenFOAM

The accuracy of the VoF methodology used in this research has been tested by conducting simulations of classic (canonical) problems with solution comparing favorably with available analytical solutions that are found in the literature (see appendix A for more details). Furthermore, an additional DNS simulation of a turbulent channel flow was conducted and results in terms of mean streamwise velocity compared favorably to the theoretical solution (refer to Chapter 4). In addition to being a typical testing problem in CFD, this turbulent channel flow simulation was needed to compute initial conditions for the DNS of coupled air-water interfacial flow which will be the focus of this thesis.

The results from these validations demonstrated the excellent agreement between the numerical solutions and the theory, which demonstrates OpenFOAM's reliability as a numerical tool capable of achieving the goals of this study.

2.6. Chapter Summary

In this chapter, physical and mathematical aspects of turbulence were reviewed and computational methodologies for tackling turbulence were discussed. DNS and LES were identified as the methodologies suitable for achieving the goals of this thesis. Details were also given about the numerical methods used in this thesis to solve the DNS and LES equations and their validation.

CHAPTER 3: MASS TRANSFER VELOCITY PARAMETRIZATION

3.1. Parametrization

Figure 3.1 exhibits a comparison between mass transfer velocities through an air-water interface determined experimentally with respect to the speed of wind at a height of 10 m above the air-water interface u_{10} from the work of Banerjee (2004). This figure shows results from one of the most frequently used parametrizations, that of Liss and Merlivat (1986) which relies solely on u_{10} to predict gas transfer velocity following:

$$k_L = 0.17u_{10} \quad \text{when } u_{10} \leq 3.6 \; m/s \tag{3.1-a}$$

$$k_L = 2.85u_{10} - 9.65 \quad \text{when } 3.6 \; m/s \leq u_{10} \leq 13 \; m/s \tag{3.1-b}$$

$$k_L = 5.9u_{10} - 49.3 \quad \text{when } u_{10} \geq 13 \; m/s \tag{3.1-c}$$

At a first glance of Figure 3.1, it is reasonable to say that these transfer velocity measurements do not indicate any strong correlation with u_{10}. The data in Figure 3.1 is scattered which indicates that there must be more than just one variable (in this case u_{10}) to explain the behavior of the transfer velocity.

Nevertheless, Wanninkhof and McGillis (1999) established a cubical fit to transfer velocity using u_{10} (equation 3.2), whereas Nightingale et al. (2000) used quadratic fit:

$$k_L = 0.078u_{10}{}^3 - 0.333u_{10}{}^2 + 1.09u_{10} \tag{3.2}$$

$$k_L = 0.222u_{10}{}^2 + 0.333u_{10} \tag{3.3}$$
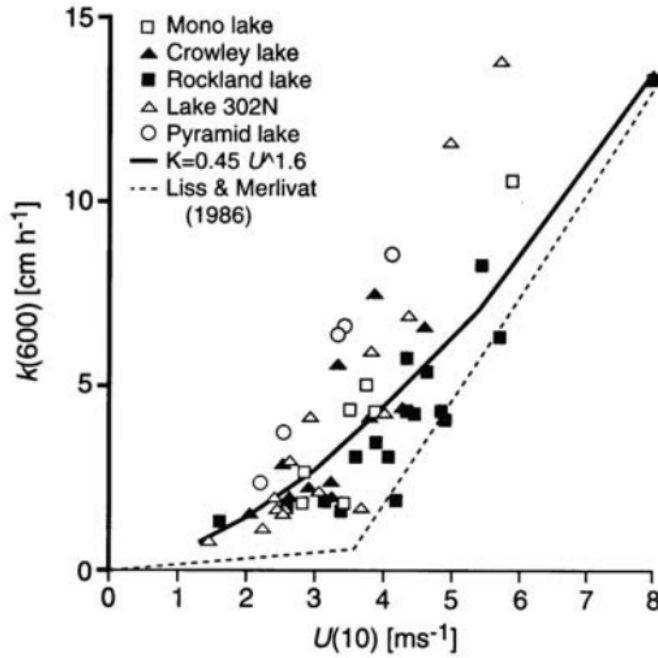
Figure 3.1 Gas transfer coefficients vs. wind speed from lakes (MacIntyre S. et al., 1995). Liss and Merlivat (1986) fit shown dotted. This figure is a reprint of Figure 6.1 from the work of Banerjee (2004).

More recently, Iwano (2013) fitted data using a combination of u_{10} raised to the powers 1.25 and 3.4 separated into two equations based on u_{10} smaller or larger than the threshold of 33.6 m/s:

$$k_L = 1.61u_{10}{}^{1.25} \quad \text{when} \quad u_{10} < 33.6 \ m/s \tag{3.4-a}$$

$$k_L = 8.43 * 10^{-4} u_{10}{}^{3.4} \quad \text{when} \quad u_{10} \geq 33.6 \, m/s \tag{3.4-b}$$

Additional parametrizations attempted to use friction velocity and significant wave height such as it is in the case of the parametrization by Woolf (2005):

$$k_L = k_0 + 2 * 10^{-5} R_H \tag{3.5}$$

where $k_0 = 1.57 \times 10^{-4} u_*$ and $R_H = u_* H_s / \nu_{water}$, u_* being the friction velocity of air, H_s is the significant wave height and ν_{water} is the kinematic viscosity of water. Recently Suzuki et al. (2015) suggested a parametrization based on fractional area of whitecap coverage:

$$k_L = 2.06 u_{10}(1 - W) + 1035W \tag{3.6}$$

where W is the fractional area of whitecap coverage and $W = 3.88 \times 10^{-7} R_B{}^{1.09}$ with R_B being the air-water Reynolds number which corresponds to $u_\tau z / \nu$ where u_τ is friction velocity due to wind stress, while ν is the molecular viscosity.

Per a technical report by Suzuki et al. (2015), using some of the parametrization models mentioned in this chapter and in Chapter 1 (i.e., equations 1.1, 1.2, 3.4-a and b, 3.5 and 3.6), the conclusion can be reached that there is a clear disagreement between all the aforementioned parametrization models. Some of the reasons behind reaching that conclusion is that all these models were empirically constructed with data collected during different conditions. Some of the variations in these conditions include differences in the margin of wind speeds considered which

may have included only low wind speeds or only high wind speeds or a combination of low and high wind speeds that may or may not have induced wave breaking, or the conducted experiments were either experiments completed in the field or in different laboratories. Moreover, as reasoned by Banerjee (2004), low predictions observed in Figure 3.1 are due to the missing representation of important factors by the parametrization used (e.g., Liss and Merlivat (1986)'s model) such as variables related to turbulent fluid motion near the deforming air water interface.

Turbulent fluid motion is known to control mass transfer through the air-water interface and therefore should be studied more as its improved understanding should lead to better parametrizations of transfer velocity. Several theories based on either turbulent or molecular diffusion attempt to better explain the behavior of mass transfer across air-water interface. These theories include the film, surface renewal, interphase mass transfer and boundary layer theories which will be discussed further in this chapter.

3.2. Mass (Scalar) Transfer Theories

3.2.1. Film Theory

Using a simplistic one-dimensional representation of convective mass transfer, film theory (Lewis and Whitman, 1924) suggests that the concentration distribution is linear within a stagnant thin film just below the air-water interface (Figure 3.2). Inside this film, gas concentration drops linearly from the concentration C_i at the interface to a bulk concentration C_{bulk} reached at the deeper end of the thin film. The concentration is constant at C_{bulk} below the thin film. Under the assumption of steady state mass transfer and low dissolved scalar (gas) concentration, a linear relationship was established, where transfer velocity is found to be directly correlated to the diffusion coefficient and inversely correlated to the thickness of the thin film:

$$k_L = D/\delta \tag{3.7}$$

where D is the molecular diffusivity of the scalar in water.
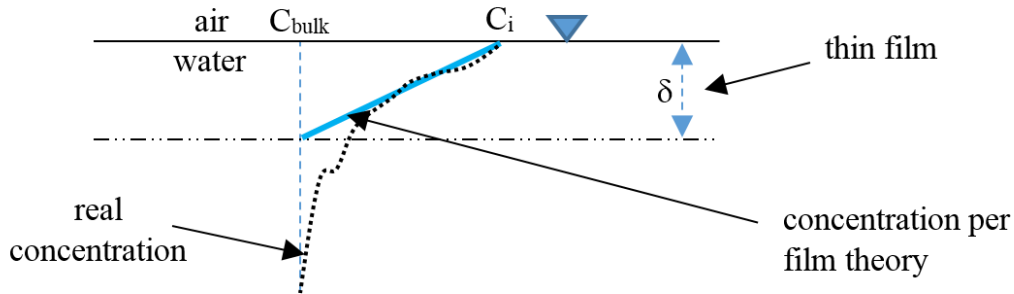
Figure 3.2 Dissolved gas (scalar) concentration profile (concentration per film theory versus actual concentration).

3.2.2. Boundary Layer Theory

In boundary layer theory both the concentration and velocity can vary in all three directions. This is in contrast with film theory in which the concentration and velocity vary in the vertical direction only. Furthermore, the change in the concentration profile in the thin film is larger in the vertical direction than in any of the other directions, thus it is sufficient to just consider diffusion in the vertical direction (Baehr and Stephan, 2006). As a result of this theory, a relationship between mass transfer velocity and molecular diffusivity is established as follows:

$$k_L \sim v^{-1/2}/D^{2/3} \tag{3.8}$$

3.2.3. Penetration Theory

Another eminent theory of mass transfer between a liquid and a gas is penetration theory. This theory, established by Higbie (1935), is based on the assumption that turbulent eddies are continuously replenishing the gas-liquid interface with low concentration fluid brought from depths of the liquid column to the surface. This renewal cycle occurs periodically within a renewal period τ_r which is particular to the characteristics of turbulence in the fluid flow. By solving the unsteady state transport equation for concentration of a dissolved gas in liquid where the only retained gradient of concentration in this equation is the one with respect to the depth while the other two gradients of concentration (i.e., with respect to the spanwise and streamwise flow directions) are considered negligible, the average mass transfer velocity k_L is found to be directly correlated with the square root of the diffusion coefficient D and inversely correlated with the renewal period τ_r:

$$k_L = 2\sqrt{\frac{D}{\pi\tau_r}} \tag{3.9}$$

3.2.4. Surface Renewal Theory

Surface renewal theory was introduced by Danckwerts (1951) who modified the penetration theory of Higbie (1935) considering that fluid elements stay at the surface for random amount of times, suggesting the use of an exponential age or contact time distribution (Toor and Marchello, 1958) as reflected by

$$\varphi(t) = se^{-st} \tag{3.10}$$

where s is the fractional rate of surface renewal due to turbulent eddies flowing between the bulk of fluid and the air-water interface, which carry low concentration fluid packages to the surface. Consequently, the average mass transfer velocity k_L is found to be directly correlated with the square root of the diffusion coefficient D and directly correlated with the square root of the fractional rate of surface renewal s (or inversely correlated with the square root of the surface renewal time scale of the turbulent eddies τ) as follows:

$$k_L = (\kappa/\tau)^{1/2} \tag{3.11}$$

Since τ depends on the turbulent characteristics of flow, it is generally parametrized in terms of turbulent kinetic energy dissipation rate ε at the surface or in terms of surface divergence which are discussed in chapter 4 in more details.

3.3. Chapter Summary

This chapter consists of a review of all different parametrization techniques used to predict mass transfer between a gas and a liquid. Conclusions arose as to why it is important to consider physically-grounded theories based on either turbulent or molecular diffusion (such as surface renewal theory) and not empirical relationships such as those based on u_{10} to better capture the behavior of gas transfer across air-water interface. In this dissertation, we will compare transfer velocity results from different parameterizations based on surface renewal theory in particular parametrizations based on near surface turbulent kinetic energy dissipation rate (Zappa et al., 2007)

and surface divergence (Banerjee, 2007) to results we obtain directly from the DNS to investigate

the accuracy of the parameterizations.

CHAPTER 4: DNS OF SCALAR (MASS) TRANSFER ACROSS AN AIR-WATER INTERFACE DURING INCEPTION OF SMALL-SCALE LANGMUIR CIRCULATION

4.1. Introduction

Turbulence associated with small scale (centimeter-scale) eddies known as Langmuir cells or LCs can have direct impact on gas uptake by oceans. During low wind speeds of 1 to 2 m/s, wave-current interaction leads to the generation of Langmuir turbulence characterized by these small scale LCs. As seen in Figure 1.2a of Chapter 1, LCs consist of parallel counter-rotating vortices roughly aligned in the direction of the wind. It is well-known that LCs result from the interaction between the Stokes drift velocity induced by surface waves and the wind-driven shear current. Recall that Figure 1.2b shows the manifestation of the LCs through the pattern in surface temperature, where elongated streaks with cold temperatures coincide with the surface convergence zones of the LCs, and elongated streaks of warmer temperatures coincide with the surface divergence zones of LCs.

In the measurements of Veron and Melville (2001) the inception of small scale LCs and subsequent transition to Langmuir turbulence (prior to the onset of micro-breaking wind waves) lead to a 70% increase in gas transfer velocity, demonstrating the strong impact of LC on gas transfer across the air-water interface. Transition to Langmuir turbulence refers to when the initially coherent vortices become unstable and loose coherency as they start to interact with each other nonlinearly. The measurements of Veron and Melville (2001) were collected under a

gradually increasing wind with final speed of 5 m/s at a fetch of 10.72 m and during the presence

of gravity-capillary waves possessing wavelengths up to 10-15 cm. More recent experiments made

with sub-surface Particle Image Velocimetry (PIV) and surface infrared radiometry were

conducted by Veron in a large air-sea interaction facility at the University of Delaware. Several

wind forcings were studied in order to obtain a variety of LC scales and intensities. It was found

that the LCs provide intense surface renewal (see Figure 4.1) and disrupt the near surface molecular

layers. In particular, the LC rapidly transport surface layers to depth thereby transporting

momentum away from the surface at rates much larger than that of molecular diffusion. Figure 4.1

presents snapshots from a video filmed in these laboratory measurements taken at two different

times, showing the progress of fluorescent dye initially deposited on the surface of a wind-driven

air-water interface as a tracer during the presence of small-scale LCs. The images are in the

crosswind-vertical plane, with the wind and waves traveling in the "into the page" direction.
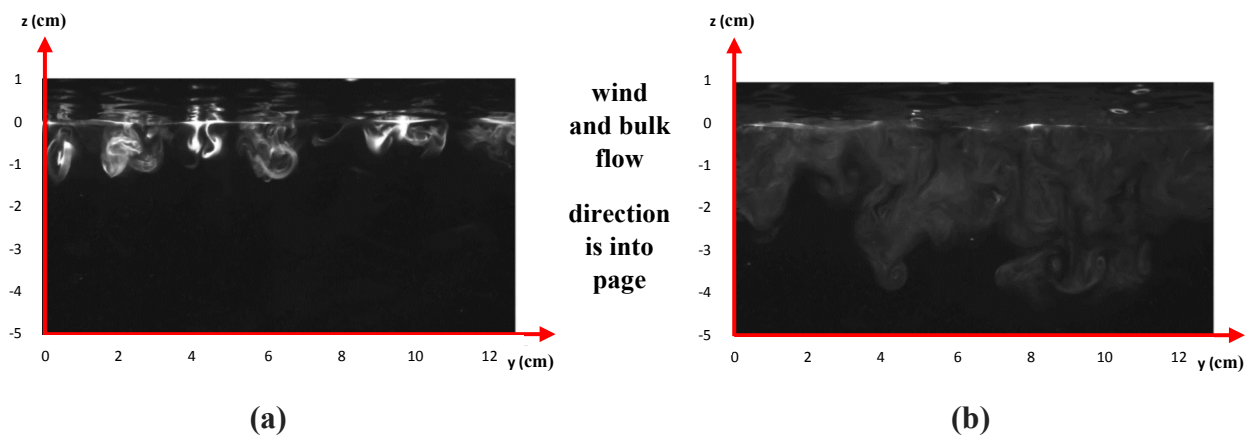
Figure 4.1 Fluorescent dye sprayed on a wind-driven air-water interface as a tracer during the presence of small-scale Langmuir cells at a) an early time, b) later time. Courtesy of Fabrice Veron, University of Delaware.

In Figure 4.1 we can see the formation of pairs of vortices which correspond to small scale Langmuir cells. By comparing the progress of the fluorescent dye within the water side between an early time (Figure 4.1a) and a later time (Figure 4.1b) the effect of Langmuir cells on vertical transport of momentum and scalars can be observed. Komori et al. (2010) performed a direct numerical simulation (DNS) similar to the laboratory setting of Veron and Melville (2001). In their DNS, LC-like structures coexisting with micro-breaking capillary waves riding on larger gravity-capillary waves were identified. However, a study of LC-like structures and their connection with gas transfer efficiency across the air-water interface was not explored.

For the present study, a similar DNS of a wind-driven coupled air-water interface was conducted focusing on the vertical transport induced by small scale LCs to further establish the connection between the cells and scalar transfer across the interface. Two simulations are compared: one with a freely deforming interface and a second one with a flat interface. In the first simulation, the deforming interface evolves in the form of gravity-capillary waves generating aqueous Langmuir turbulence characterized by small scale LCs. The second simulation is characterized by pure shear-driven turbulence in the absences of LCs as the interface is intentionally held flat

4.2. Governing DNS Equations

The DNS equations consist of the incompressible continuity and the Navier-Stokes equations:

$$\frac{\partial u_i}{\partial x_i} = 0 \tag{4.1}$$

$$\frac{\partial u_i}{\partial t} + u_j \frac{\partial u_i}{\partial x_j} = -\frac{1}{\rho}\frac{\partial p}{\partial x_i} + \nu \frac{\partial^2 u_i}{\partial x_j^2} \tag{4.2}$$

33

where u_i denotes the velocity field (i = 1, 2 and 3 represent the streamwise (or downwind), spanwise and vertical components, respectively), p is the pressure field, ν is the molecular kinematic viscosity and ρ is the density. In addition to the continuity and momentum (Navier-Stokes) equations to predict air and water flow velocities and pressures, the concentration of dissolved scalar (i.e. gas) in air and in water is predicted via an additional scalar transport equation:

$$\frac{\partial C}{\partial t} + u_j \frac{\partial C}{\partial x_j} = \kappa \frac{\partial^2 C}{\partial x_j^2}$$

(4.3)

where C is the concentration of the scalar and κ is the molecular diffusivity of the scalar. In this study, as has been done in others, the ratio ν/κ or Schmidt number (Sc) is set to 1 because this does not affect the fundamental turbulent mechanisms promoting scalar transfer across the interface.

Simulations conducted follow closely the recent DNS of Komori et al. (2010) of wind-driven, coupled air-water molecular boundary layers with a nonlinearly deformable surface (interface). The juxtaposed domains of the air and water fluids along an initially flat gas-liquid interface are represented by rectangular boxes with depths of δ and 2δ respectively, where $\delta = 1.25$cm, while the streamwise and spanwise lengths are 8δ and 4δ respectively (see Figure 4.2.a). A Cartesian coordinate system was adopted where the streamwise and spanwise directions are given by the x-axis and the y-axis respectively, while the z-axis spans the air and water depths (see computational domain in Figure 4.2.a).

34
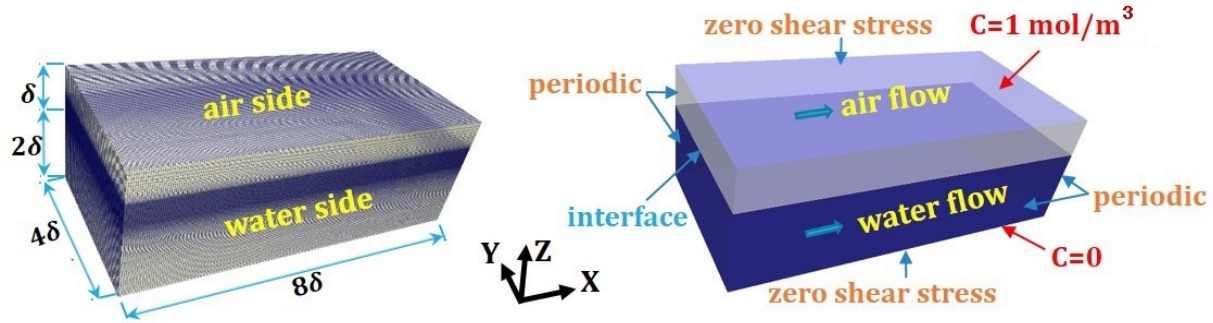
Figure 4.2 a) Coupled air-water flow domain and computational mesh and b) flow domain and boundary conditions: Zero shear stress with zero normal flow and prescribed scalar concentration at top and bottom of the domain; periodicity in streamwise and spanwise directions.

The water side in this simulation is started from rest with a flat air-water interface driven from above by the sudden imposition of a pre-computed, fully-developed boundary layer airflow driven by a pressure gradient with zero shear stress at the top and periodic streamwise and spanwise faces. This boundary layer airflow was pre-computed as a first step, in a separate simulation with a no-slip bottom and a zero-shear stress condition on top while maintaining periodic boundary conditions elsewhere (along streamwise and spanwise boundaries). The pre-computed airflow was characterized by far-field mean velocity $U\infty = 5$ m/s which is the same as the final wind speed in the experiments of Veron and Melville (2001). The initial condition for scalar concentration was $C = 1$ mol/m^3) in the air side and $C = 0$ in the water side. At the top of the domain (at the top of the air side) C was set to 1 mol/ m^3 and at the bottom of the domain (the bottom of the water side) C was set to 0, ensuring a flux of scalar from the air side to the water side (Figure 4.2.b).

The simulated Reynolds number based on $U\infty$, and the height of the air column, δ, is 4160. The Reynolds number based on the air-side friction velocity at the air-water interface, u_τ, and δ is 200. Given this modest Reynolds number, we have ensured that the distances from the air-water

interface to the closest grid points on the water and air sides, Δz, are less than $\Delta z+ = 1$, where $\Delta z+ = u_\tau \Delta z / v$ with u_τ and v being the friction velocity and kinematic viscosity, respectively, in the water side or air side. Thus, the closest grid points to the air-water interface fall within the molecular sub-layer (see Appendix B for definition) either on the air or water sides. As such, the air and water-side regions near the air-water interface have DNS-level resolution and do not require a subgrid-scale large-eddy simulation model. The grid points used in the streamwise, spanwise and vertical directions of the computational domain were 200 by 100 by 60 on the air side and 200 by 100 by 120 on the water side. The grid resolution for this mesh is between the order of 0.006 centimeters (within the air-water interface) and 0.05 centimeters (near the top and bottom of the air side). The computational mesh is chosen as uniform along the streamwise and spanwise directions while a non-uniform gradually refined meshing scheme was applied starting from the top surface of the air column down to the air-water interface and from the bottom surface of the water column up to the air-water interface. This meshing scheme was purposely used to heavily refine the air-water interfacial region of interest in order to capture the centimeter-scale interfacial deformations as well as the molecular sub-layers in the air and water sides.

4.3. Preliminary Simulation to Obtain Initial Condition

As mentioned earlier, a simulation of solely airflow was necessary to fully develop the turbulent airflow that will be superimposed above a flat interface separating the air side and the water side to start the two-phase air-water DNS simulation. For consistency, the computational mesh to run the preliminary airflow simulation was made identical to the air side portion of the air-water mesh in Figure 4.2.a. This simulation also serves as a validation test of the OpenFOAM finite volume solver of this study. The turbulent airflow was driven by a body force of approxima-

tely 6.024 N/m^3 in the x-direction which corresponds to an air friction velocity of $u_\tau = 0.25$ m/s and leading to a final free stream wind speed of $U_\infty = 5.0 \, m/s$. The top of the domain was characterized by imposed zero shear stress and the bottom by no-slip. Periodicity was set in the streamwise and spanwise directions. The mesh was designed to resolve the bottom viscous boundary layer as described earlier. Furthermore, the time step was chosen so that the Courant Friedrichs Lewy (CFL) number is smaller than unity for all times to ensure that a fluid parcel is not allowed to move more than one grid spacing for each time step avoiding numerical instabilities (Courant et al. 1967). This simulation ran long enough until its combined resolved (Reynolds and mean viscous) stresses matched expected results from theory (Pope, 2000).
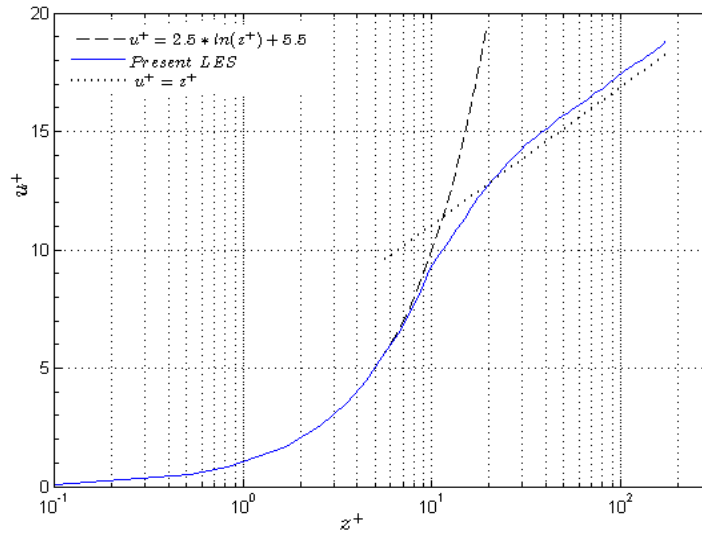

Figure 4.3 Mean streamwise velocity.

Figure 4.3 shows the mean streamwise velocity profile, non-dimensionalized in so-called wall or plus units defined as $u^+ = \langle u \rangle / u_\tau$ where the bracket denotes averaging in time and over

spanwise and streamwise directions. Figure 4.3 shows this velocity versus the dimensionless

distance to the bottom no-slip wall in plus units defined as $z^+ = u_\tau z / \nu$.

The dashed lines in Figure 4.3 above represent the theoretical law of the wall and the log

law. The simulated mean streamwise velocity distribution overall is in excellent agreement with

the theoretical solution (details of the expected turbulent boundary layer structure and the mean

streamwise velocity distribution versus u^+ are found in Appendix B) . Indeed, within the viscous

sub-layer, which is the nearest region to the wall , where molecular viscosity is predominant in

momentum transport while turbulence is negligible, the mean streamwise velocity follows a linear

correlation with the wall distance up to $z^+ = 5$ (Tennekes et al., 1972). Furthermore, the buffer

sub-layer, which corresponds to a blending region where both turbulence and molecular viscosity

are important in momentum transport is observed from $z^+ = 5$ until approximately $z^+ = 30$

where the mean streamwise velocity transitions to a logarithmic correlation (linear in the semilog

representation) with the wall distance (Tennekes et al., 1972). Beyond $z^+ = 30$, a logarithmic

correlation between the mean streamwise velocity and the wall distance is observed, where

turbulent regime is predominant in momentum transport while viscous effects are negligible. This

region is represented by a theoretical equation as follows

$$u^+ = \frac{1}{\kappa}\ln(z^+) + B \qquad\qquad (4.4)$$

where the von Karman coefficient is $\kappa = 0.41$ and the coefficient $B \approx 5.5$ (Schlichting, 1960). A

small discrepancy between the simulated mean streamwise velocity and the theoretical log-law

was observed, potentially due to a low-Reynolds number effect given that the the the theoretical log-

law is derived for Reynolds number much higher than the Reynolds number of the simulation (200) .

The excellent agreement between the computed mean velocity and the theoretical velocity throughout the boundary layer shows that the DNS mesh is able to accurately resolve (capture) the boundary layer dynamics important for determining the gas transfer across analogous boundary layer regions above and below the air-water interface in DNS of the coupled air-water flow presented next.

4.4. Simulation of Coupled Air-water Flow

The fully developed boundary layer airflow characterized by air friction velocity of $u_\tau = 0.25$ m/s and free stream air speed of $u_\infty = 5\ m/s$ obtained in the previous simulation (section 4.1) was superimposed on the air portion of the computational mesh in Figure 4.2 while the water portion is started from rest with a flat air-water interface. The top and bottom boundary conditions applied to the computational domain are zero-shear stress. This DNS was performed with a CFL condition of at least 0.25 maintained throughout the simulation which corresponds to the VoF methodology limitation as suggested by Wardle (2008). Figure 4.4.a shows the initial condition of the air-water interface coupled simulation. The figure shows that the simulated wind speed has a magnitude of approximately $u_\infty = 5$ m/s (red corresponds to this value) at the top of the air side and decreases as the boundary layer reaches the air-water interface.

Figure 4.4.b shows an instantaneous snapshot of streamwise (x) velocity field distribution within the domain showing the turbulence in action within both the air side and the water side at t=5 seconds. Note the air flow velocities are much higher than the water flow velocities as expected.

(a)　　　　　　　　　　　　　　　(b)
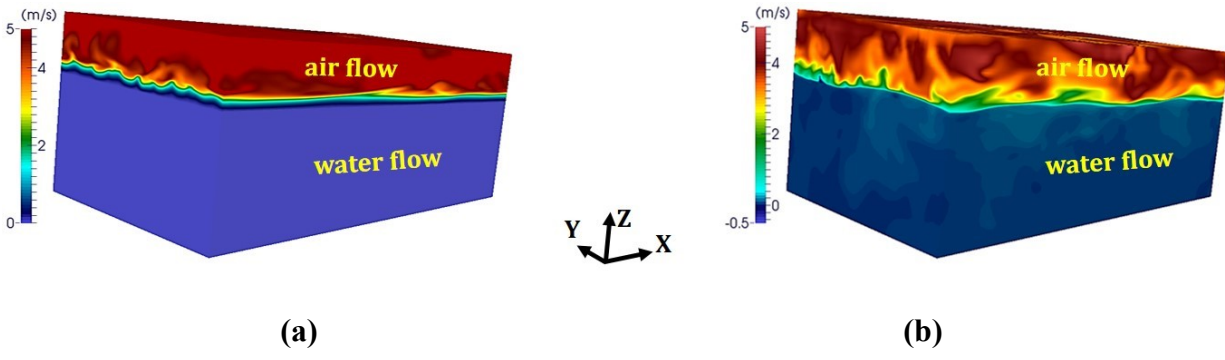
Figure 4.4 a) Instantaneous snapshot of streamwise (x) velocity field distribution within the domain showing the turbulence in action within the air side and the water at rest as initial conditions and b) Instantaneous snapshot of streamwise velocity field distribution within the domain showing turbulence in action within both the air and water sides after 5s.

4.5. Small-scale Capillary Waves (Ripples)

Soon after the simulation started, at time $t = 1.5s$, short gravity-capillary waves as small as one centimeter in wavelength and 0.25 millimeters in height are present accompanied by small capillary waves (ripples) with length scales around 1 to 2 millimeters.

(a)　　　　　　　　　　　　　　　(b)
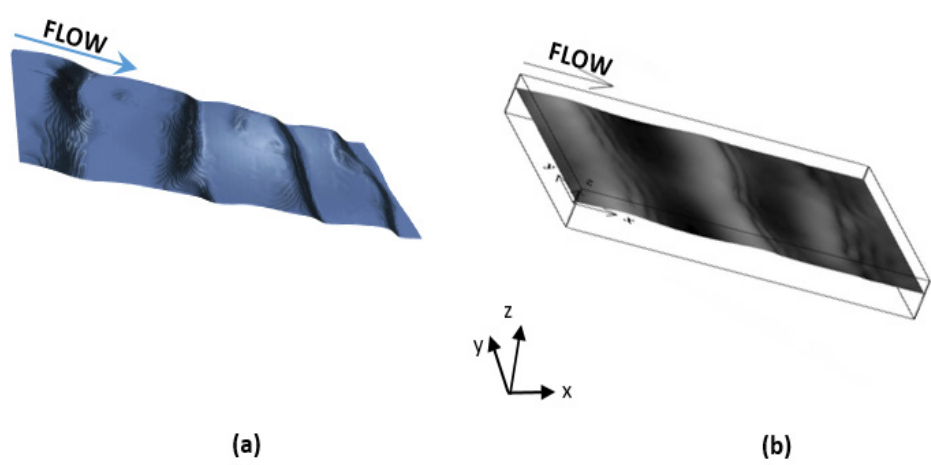
Figure 4.5 Instantaneous air-water interface: a) present DNS at t=2.5s and b) Komori et al. (2010) at   t=6.5s.

Figure 4.5.a shows a snapshot of the air-water interface deformation (corresponding to simulation time $t = 2.5s$) of the present DNS revealing gravity-capillary waves along with superimposed smaller capillary waves or ripples. Figure 4.5.b illustrates the captured waves and ripples in the Komori et al.(2010) DNS at their simulation time $t = 6.5s$ .Similar to the results of Komori et al (2010), it has been observed in the present DNS that the simulated capillary waves are slightly non-uniform in the spanwise direction while ripples are localized on the forward face just below the gravity waves that carry them (Figure 4.5.a and b). According to Hung and Tsai (2009) the beginning of the formation of these ripples is characterized by a localized pressure disturbance on the forward side of the carrier wave near the crest which develops an oscillatory train of capillary waves. Hung and Tsai (2009) suggest the existence of a minimum crest curvature threshold (0.25 cm^{-1}) of the carrier wave for the formation of the ripples to take place, and this threshold curvature is almost independent of the carrier wavelength.

4.6. Quantification of Interface Wave Height and Water Velocity On the Interface

During the simulation, a time series of maximum wave height of the air-water interface was recorded where for each selected time step the maximum wave height corresponds to the highest air-water interface elevation simulated, shown in Figure 4.6.a. The evolution of the simulated gravity waves compares well with the results from the DNS of Komori et al. (2010) (Figure 4.7.a) since both time series of the air-water maximum wave height were found to follow the same trend. In order to avoid excessive storage requirement while completing this study, only approximately 40 computation steps were used to plot the general trend of the wave heights which explains why the simulated curve does not exhibit the fluctuations of the wave height evolution seen in the Komori et al. DNS. Also, the difference in time to reach a wave height of $\delta/4$ ($0.32\ cm$)

between the present DNS and the DNS of Komori et al. (2010) is about one second and this difference is perhaps due to the different numerical methodologies used. Note that Komori et al. (2010) used the marker and cell (MAC) method to solve the governing equations (Harlow and Welch, 1965) while they tracked the air-water interface using an arbitrary Lagrangian-Eulerian approach with a moving grid.

The time series in Figures 4.6 and 4.7 end at $t{\sim}8$ s, which corresponds to the end of the simulations. Komori et al. (2010) argued that for the extent of the model domain adopted, the DNS should run until the wave height reaches $\delta/4$ which corresponds to approximately 0.32 cm to ensure that the effect of the boundary conditions on the wind waves is minimal. This criterion has been used in the present DNS to stop the simulation.

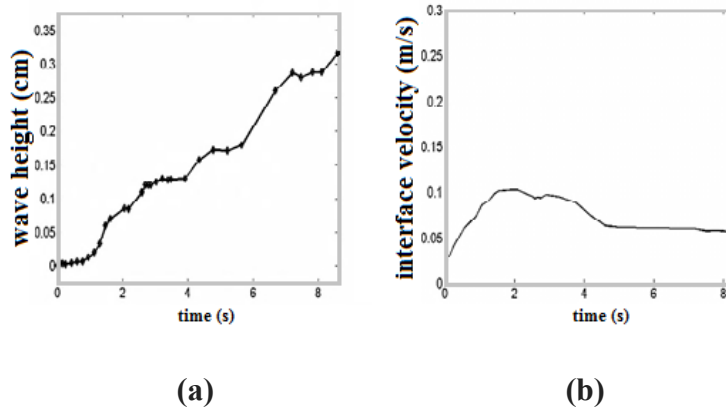(a)   (b)

Figure 4.6 (a) Time series of maximum air-water interfacial wave heights simulated in the present DNS; (b) Time series of average streamwise velocity on the air-water interface, simulated in the present DNS.
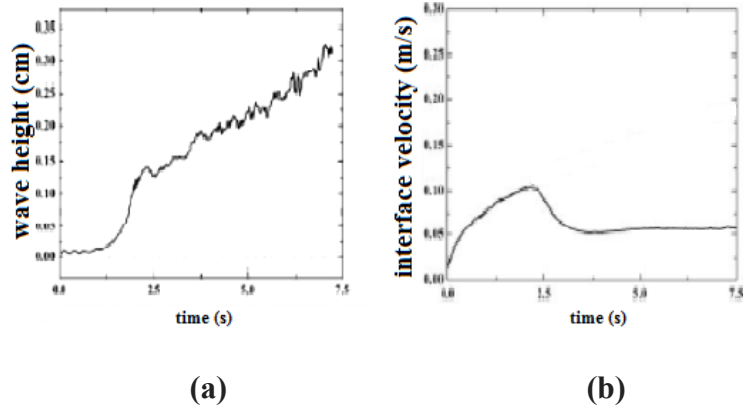
42

Figure 4.7 (a) Time series of maximum air-water interfacial wave heights, simulated by Komori et al., 2010; (b) Time series of average streamwise velocity on the air-water interface, simulated by Komori et al., 2010.

The average streamwise velocity of the grid cells that fall halfway between the air and water sides (representative of downwind velocity at the interface) were also plotted to compare with Komori et al.'s DNS results. Per Figures 4.6.b and 4.7.b, the interfacial velocities reached a maximum velocity of approximately 0.1 m/s in both the current DNS and DNS of Komori et al. The shapes of these velocity curves were also found to be similar. In both cases, a sharp increase of the air-water interfacial velocity is observed until reaching its maximum in a span of two seconds, followed by a decrease, after which the interfacial velocity stabilizes at approximately half of its maximum.

4.7. Turbulence Structure and Scalar Flux

During the early stages of the DNS of the coupled air-water interface, a coherent structure is observed in terms of streamwise velocity fluctuation at the interface, even though the capillary wave deformation was not yet noticeable. As early as time $t = 0.5$ s, the DNS streamwise velocity fluctuation, displayed on the instantaneous air-water interface in Figure 4.8.a, exhibits narrow smooth downwind elongated streaks. These narrow streaks are found to be parallel to each other

and alternate in sign in the spanwise direction. The fluctuation is obtained by subtracting the mean velocity (averaged over the interface) from the velocity on the interface.
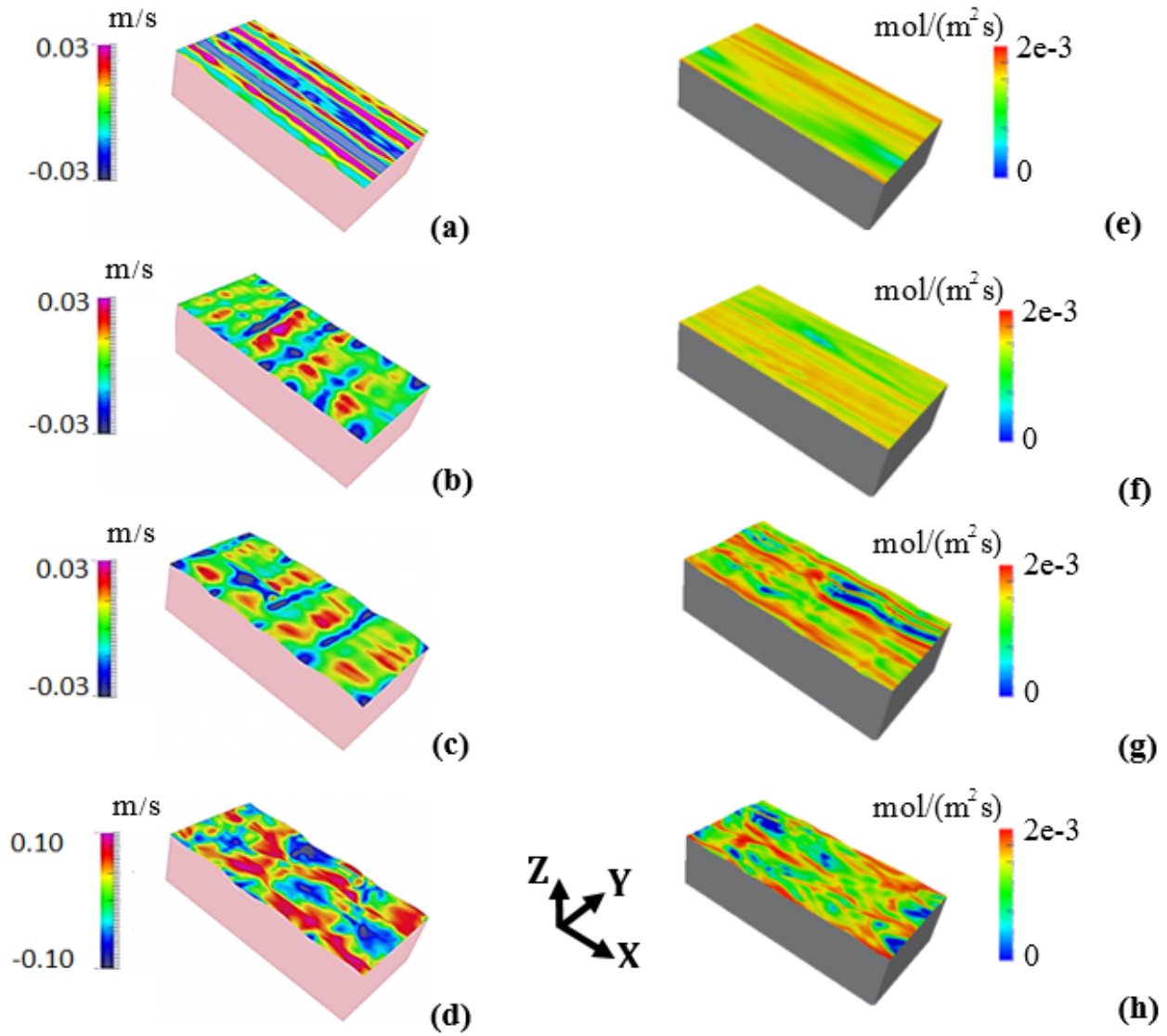

Figure 4.8 Instantaneous streamwise velocity fluctuation in m/s at a) $t = 0.5$ s, b) $t = 1$ s c) $t = 2.5$ s and d) $t = 4$ s and Instantaneous scalar flux in mol/(m²s) at e) $t = 0.5$ s and f) $t = 1$ s g) $t = 2.5$ s and h) $t = 4$ s.

These narrowly-spaced downwind-elongated streaks are associated with coherent small-scale vortices or small scale LCs within the emerging turbulent boundary layer on the water side. These vortices will be revealed further below in terms of streamwise vorticity. The positive streaks correspond to the surface convergence zones of the small scale LCs resolved and result in an acceleration of the local downwind bulk flow similar to the downwind acceleration usually observed over the surface convergence zones of the much larger Langmuir cells typically observed spanning the ocean surface mixed layer (e.g. see Thorpe, 2004). Soon after the start of the growth of capillary waves, starting at approximately $t = 1$ s (Figure 4.8b), it was observed that the streaky structure of the streamwise velocity fluctuation was disrupted by the capillary wave deformations until about $t = 2.5$ s (Figure 4.8c). This disruption is due to the fact that the downwind velocity fluctuation not only has a component from the turbulence but it also includes a significant gravity-capillary wave-induced component. As time progresses beyond t=2.5 s, (e.g. at $t = 4$ s, Figure 4.8d) the downwind elongated streaks re-emerge, due to the turbulent component of the velocity becoming more dominant than the wave-induced component. This re-emergence of the downwind elongated streaks is indicative of the flow transitioning to Langmuir turbulence.

Figures 4.8.e-h show instantaneous scalar molecular fluxes at the air-water interface at $t = 1$ s, $t = 2.5$ s, $t = 4$ s and $t = 6$ s. This flux can be obtained as

$$F = \kappa \nabla C \cdot \boldsymbol{n} \tag{4.5}$$

evaluated at the air-water interface, where $\boldsymbol{n}$ is the normal to the interface. As seen in Figures 4.8.e-h, the flux shows an increase for simulation times greater than $t = 2.5\ s$, attributed to the

transition to Langmuir turbulence previously described. Note that the flux is characterized by streaks similar to the velocity fluctuations, suggesting strong correlation between the turbulence and the flux.

Vorticity of the flow was computed following its mathematical representation defined as the curl of the velocity field $\vec{u}$ as follows:

$$\vec{\omega} = \nabla \times \vec{u} \tag{4.6}$$

Additionally, we compare results in terms of instantaneous streamwise vorticity in our DNS of the air-water interface (deforming case) with instantaneous streamwise vorticity coming from a similar simulation but with the air-water interface held fixed (flat).
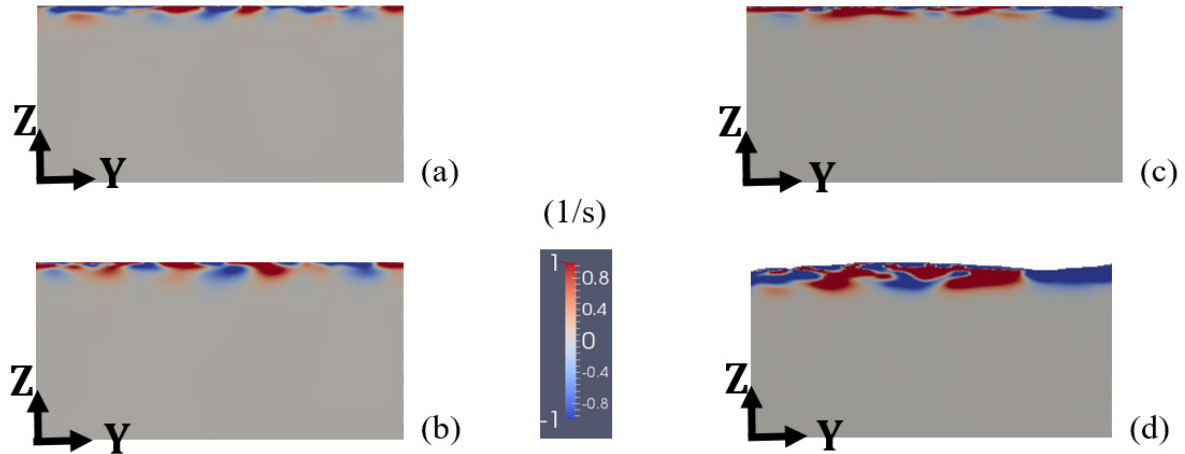

Figure 4.9 Instantaneous streamwise vorticity (1/s) from DNS with air-water interface held flat at a) $t = 1$s and b) $t = 3$s and instantaneous streamwise vorticity (1/s) from DNS with freely deforming air-water interface at c) $t = 1$s and d) $t = 3$s.

The results from the flat interface case are shown on Figures 4.9.a and 4.9.b and the results from the deforming interface case are shown on Figures 4.9.c and 4.9.d. The deforming interface case is characterized by Langmuir cells growing in the cross-stream direction and in depth whereas the simulation with the flat interface shows smaller and less intense near-surface vortices. A random spanwise-vertical cross section was selected at $t = 2.5$ s from the start of the deforming interface case to have a look at the correlation between velocity and vorticity fields. Figure 4.10 shows spanwise velocity and streamwise vorticity in order to further elucidate the structure beneath the streamwise streaks presented earlier. For example the surface convergence of vortices is characterized by convergence of positive and negative spanwise velocity fluctuation giving rise to the downwelling limbs of the vortices beneath.
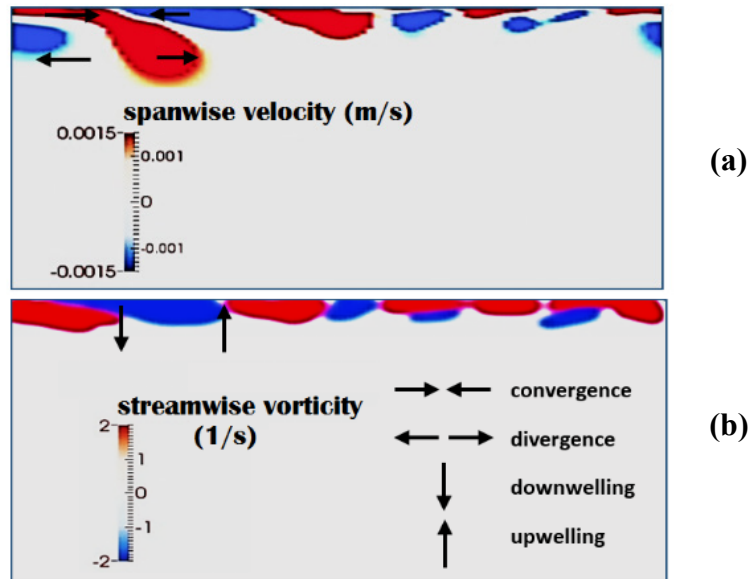

Figure 4.10 Instantaneous ($t = 2.5$s) a) spanwise velocity, b) streamwise vorticity. In panel (a) arrows denote the surface convergence and bottom convergence zones of the LCs. In panel (b), arrows denote the downwelling and upwelling limbs of the LCs.

Moreover, prior to the transition to Langmuir turbulence in the freely-deforming interface case which was previously determined to be at approximately t=2.5 s, both cases simulated (flat and deforming interface simulations) were compared in terms of depth profiles of mean scalar concentration in the water column. It was found that both cases possess similar concentration profiles through $t = 2.5$ seconds (not shown). However, for times greater than 2.5 seconds, the Langmuir turbulence and associated Langmuir cells in the deforming interface case generate greater vertical transport than the purely shear generated turbulence in the flat interface case. From the depth profiles and instantaneous contours of scalar concentration shown in Figure 4.11, we can conclude that the Langmuir turbulence penetrates deeper than the shear turbulence thus the Langmuir turbulence is able to transport higher concentration fluid to greater depths. Note that as time progresses the difference between Langmuir turbulence penetration in the deforming interface case and the shear turbulence penetration in the flat interface case becomes more significant.
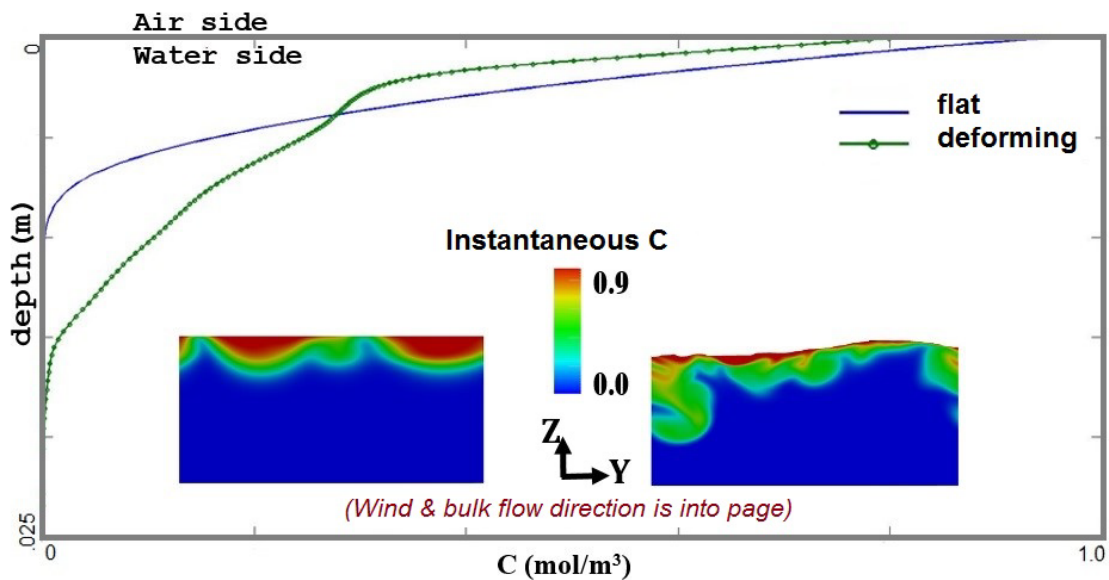
Figure 4.11 Depth profiles (averaged over streamwise and spanwise directions) and instantaneous snapshots of scalar concentration at time $t = 4s$ in the simulation with a deforming interface and the simulation with a flat interface.

48

The spatially averaged scalar flux across the wind-driven air-water interface for the flat and deforming interface cases are shown in Figure 4.12. A dramatic explosion or spike of scalar flux is observed in the deforming case at approximately $t = 2.5$ s when the flow transitions to Langmuir turbulence. In contrast, this sudden increase in scalar flux is noticeably absent in the flat interface case. After this spike, the average scalar flux obtained in the deforming interface case decreases significantly but stabilizes at a mean value approximately five times greater than the scalar flux obtained in the flat interface case. In the field, it is likely that such gas flux spikes are correlated with wind transients or gusts and thus might be a dominant contributor to the long-term time-averaged gas flux as postulated by Veron and Melville in their laboratory experiments exhibiting this same phenomena.
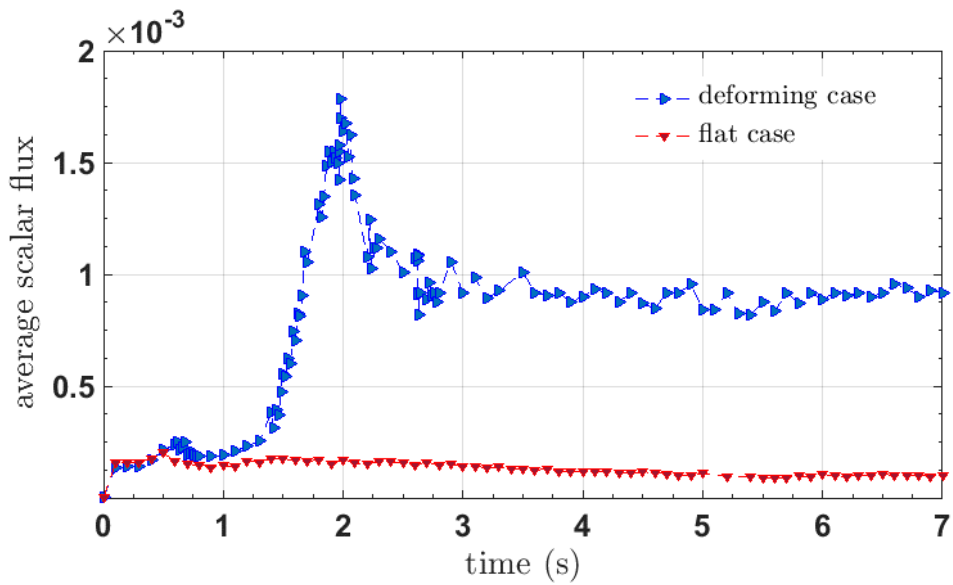
Figure 4.12 Average scalar flux through the air-water interface.

4.8. Transfer Velocity

We calculate transfer velocity, a measure of scalar transfer efficiency, following Kader et al. (1972), as

$$k_L = \kappa \frac{\nabla C \cdot n}{(C_i - C_{bulk})} \tag{4.7}$$

where C_i is streamwise and spanwise average concentration on the interface and C_{bulk} is bulk concentration calculated as

$$C_{bulk} = \int_0^{2\delta} \langle C \rangle_{x,y} \langle u_1 \rangle_{x,y} dz \tag{4.8}$$

with $\langle \cdot \rangle_{x,y}$ denoting the average over streamwise and spanwise directions. Due to the enhanced vertical transport induced by the Langmuir turbulence and associated cells, the bulk concentration is greater in the interface deforming case compared to the flat interface case (Figure 4.13).
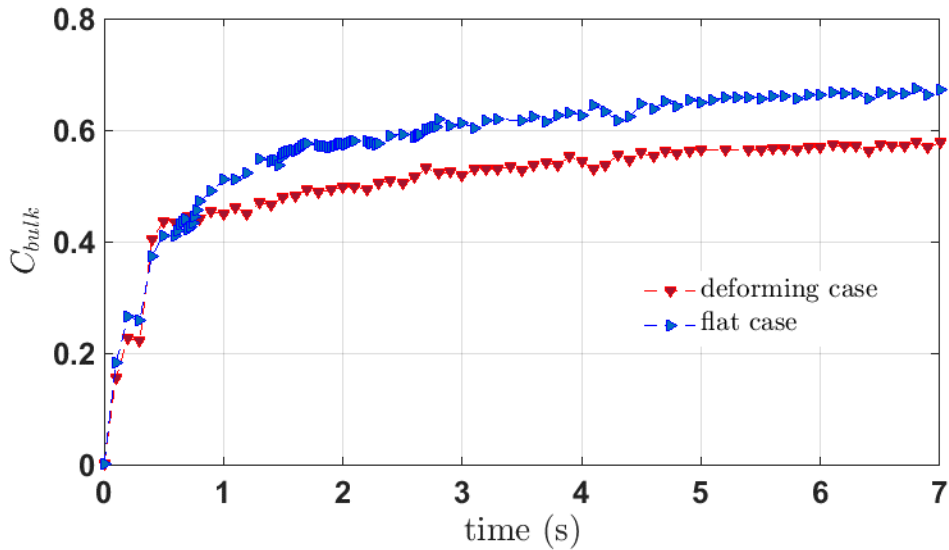
Figure 4.13 Bulk concentration of the air-water interface.
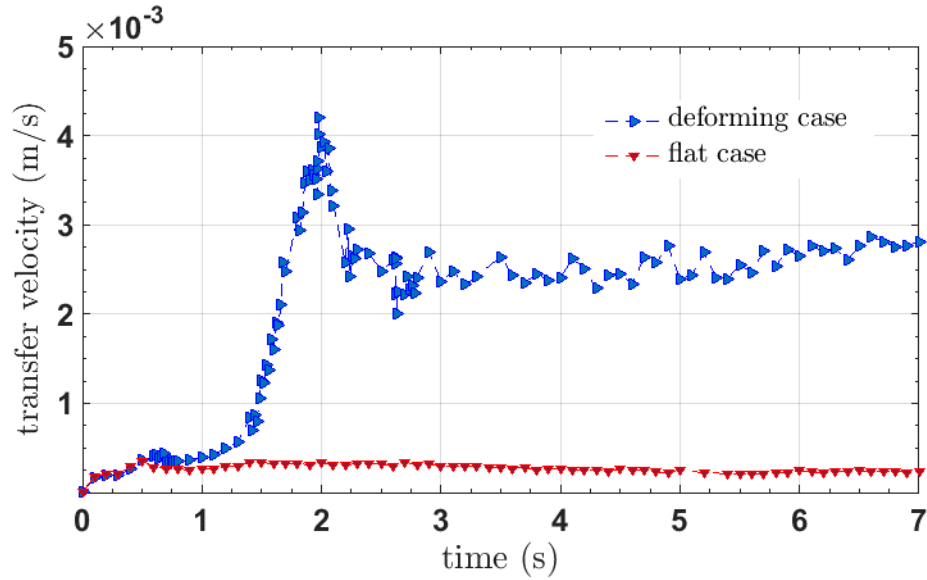
Figure 4.14 Transfer velocity.

Ultimately this leads to a greater transfer velocity (k_L) in the deforming interface case (Figure 4.14), as k_L is inversely proportional to the difference between concentration at the interface and bulk concentration (Eq. 4.5). In the field, direct evaluation of scalar flux via Eq. (4.5) is impractical and instead following Eq. (4.7), the flux is evaluated as a parameterized transfer velocity multiplied by the difference in concentration at the interface and the bulk, $(C_i - C_{bulk})$.

4.9. Parametrization

As discussed in Chapter 1 and Chapter 3, it was established that surface renewal theory is one of the most solid theories used to parameterize transfer velocity k_L. This theory is based on the principle that turbulent eddies bring up low concentration fluid packages from below intermittently. Recall that, according to the surface renewal theory, transfer velocity can be obtained from the diffusivity D and from knowledge about the surface renewal time scale of the turbulent eddies τ following equation 4.9.1.

$$k_L = (D/\tau)^{1/2} \qquad\qquad (4.9)$$

Two parametrization models to estimate τ are based on near surface turbulent kinetic energy dissipation rate (Zappa et al., 2007) and surface divergence (Banerjee,2007), respectively. These models are more physically grounded compared to the widely used models obtained from empirical relationships purely based on wind speed disregarding other important physical processes known to play important roles. For example, in the experimental work of Zappa et al. (2007), turbulent kinetic energy (TKE) dissipation at or near the air-air water interface is seen to be positively correlated with gas transfer velocity, suggesting that a transfer velocity model should be given in term of TKE dissipation at the surface. In the next sub-sections, the small eddy model (based on surface TKE dissipation) and the surface divergence model will be introduced. Following that, and using the results of the DNS, the accuracy of these models is examined, including investigating their different predictions of the spike in transfer velocity during the transition of the flow to Langmuir turbulence as observed on Figure 4.14.

4.9.1. Small Eddy Model

Assuming that small near-surface eddies control the surface renewal, Banerjee et al. (1968) proposed a parameterization of τ in terms turbulent kinetic energy dissipation rate ε at the surface defined as:

$$\tau \propto (v/\varepsilon)^{1/2} \qquad\qquad (4.10)$$

where ε is defined as

$$\varepsilon = \nu \left\langle \frac{\partial u_i'}{\partial x_j} \frac{\partial u_i'}{\partial x_j} \right\rangle \tag{4.11}$$

evaluated at the surface. Inserting (4.10) into Eqn. (4.9.1) leads to the small eddy model with a parameter or coefficient due the proportionality in (4.10). Zappa et al. (2007) used a large field experimental data set collected under a wide range of wind and wave conditions and determined the following final expression:

$$k_L = 0.419(\varepsilon \nu)^{1/4} Sc^{-1/2} \tag{4.12}$$

4.9.2. Surface Divergence Model

An alternative surface renewal time scale was proposed by McCready et al. (1986) in terms of surface divergence as

$$\tau \propto < \beta^2 >^{-1/2}$$

(4.13)

where the surface divergence β corresponds to:

$$\beta = -\frac{\partial u_3'}{\partial x_3} \tag{4.14}$$

evaluated at the water surface. Inserting (4.14) into (4.13) and using (4.9) leads to the surface divergence model:

$$k_L = 0.71v^{1/2} < \beta^2 >^{1/4} Sc^{-1/2} \qquad (4.15)$$

with 0.71 being the constant of proportionality associated with (4.13).

4.9.3. Parametrization Results

Using the results of the DNS, investigating the accuracy of parameterizations of gas transfer velocity via the small eddy model and the surface divergence model, especially their prediction of the spike in transfer velocity during the transition of the flow to Langmuir turbulence is possible. As seen in Figure 4.15, prior to this transition both models agree well with the DNS. The peak of the transfer velocity is best predicted by the surface divergence model whereas the small eddy model underpredicts the peak by 19%. After the peak, the surface divergence model slightly overpredicts while the small eddy model underpredicts the transfer velocity.
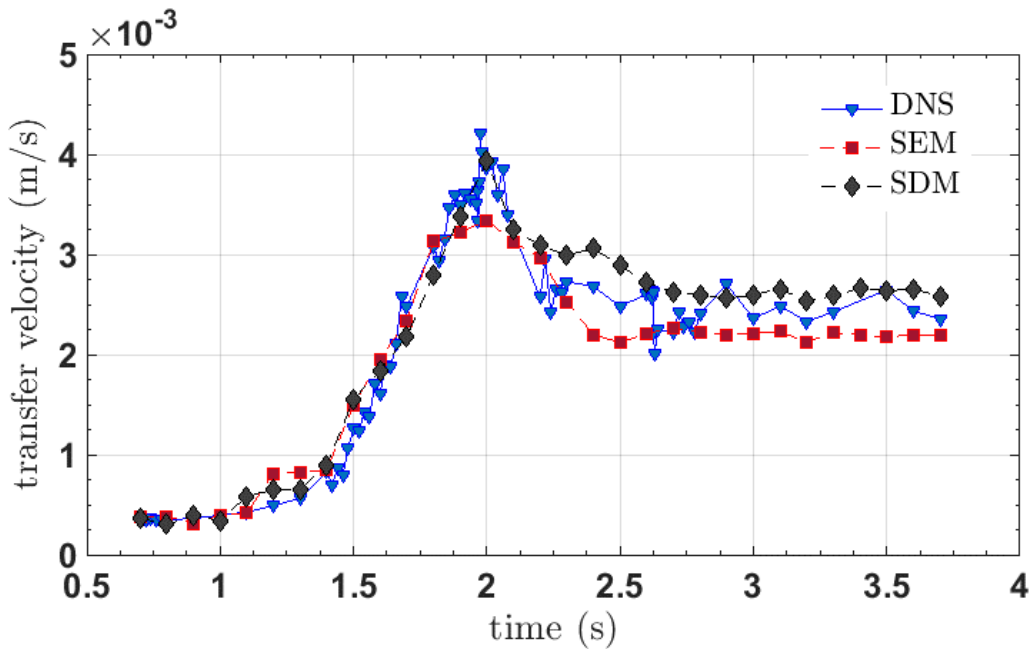

Figure 4.15 Comparison of transfer velocity in the DNS (defined in Eq. (4)) with modelled transfer velocity predicted via the SEM in Eq. (9) and via the SDM in Eq. (12).

4.10. Chapter Summary

In this chapter a DNS of a wind-driven coupled air-water interface with resolution of gravity-capillary waves and molecular sublayers below and above the interface similar to Komori et al. (2010) was conducted following a thorough validation process. For example, results from the present DNS compared favorably to the DNS of Komori et al. (2010) in terms of evolution of the air-water interface waves and the streamwise velocity at the air-water interface.

Transfer of scalar (mass) from the air to the water side in the DNS was ensured by saturating the air side with the scalar. It was seen that the deforming interface and associated aqueous Langmuir turbulence plays an important role in determining vertical transport of the scalar throughout the water side. Vertical transport induced by the LCs was seen to enhance bulk concentration throughout the water column which ultimately enhances transfer velocity, a measure of scalar transfer efficiency. LCs rapidly transport surface layers to depth thereby transporting momentum and scalars away from the surface at rates much larger than shear-driven turbulence occurring when the air-water interface was intentionally held flat.

Transition to Langmuir turbulence was observed to be accompanied by a spike in scalar (mass) flux characterized by an order of magnitude increase. These flux increases, if linked to episodic gusts and unsteadiness in the wind field, are expected to be an important contributor in determining the long-term average of the air-sea fluxes. Thus, these results highlight a new (pressing) need of developing practical parameterizations of transfer velocity that can capture scalar flux spikes associated with transition to Langmuir turbulence on the sea surface during sudden wind gusts. Although parameterizations of the transfer velocity such as the small eddy model and surface divergence model were seen to be able to capture the spike, these parameteriza-

tions require knowledge of the turbulence, for example, in terms of the surface TKE dissipation rate and the surface divergence. More practical parameterizations of the transfer velocity have been developed in terms of easily accessible parameters such as wind speed, however, such a parameterization would not be able to capture the spike in scalar transfer as a result of the transition to Langmuir turbulence. In the cases studied here, the spike in scalar flux occurred during transition to turbulence while the mean far-field wind speed was constant at $5\,\mathrm{m\,s^{-1}}$, thus the wind speed would not be able to serve as a proxy for the spike in transfer velocity.

Finally, recent DNS studies by Takagaki et al. (2015) have shown that the surface shear turbulence of smaller scale than the LCs is the primary factor in driving scalar transfer across the air-water interface via molecular diffusion. Nevertheless, the DNS case investigated here with gravity-capillary waves and associated Langmuir turbulence is characterized by a spike in scalar transfer unlike the DNS case without waves and LCs (i.e. when the air-water interface is intentionally held flat). Furthermore, after the passage of the scalar flux spike, the scalar flux remained higher (by a factor of five) in the case with waves and LCs unlike the case with air-water interface held flat. Thus, the upcoming chapter will focus on understanding the cause of this and thus the influence of the waves on the small scale shear-turbulence (smaller than the LCs) that controls the scalar transfer across the air-water interface via molecular diffusion.

CHAPTER 5: IMPORTANCE OF LANGMUIR CELLS IN SCALAR FLUX

5.1. Introduction

Recent DNS studies by Takagaki et al. (2015) have shown that the surface shear turbulence of smaller scale than the LCs is the primary factor in driving scalar transfer across the air-water interface via molecular diffusion. Nevertheless, as seen in Chapter 4, the DNS case investigated with gravity-capillary waves and associated Langmuir turbulence is characterized by a spike in scalar transfer unlike the DNS case without waves and LCs (i.e. when the air-water interface is intentionally held flat). Additionally, after the passage of the scalar flux spike, the scalar flux remained higher (by factor of five) in the case with waves and LCs unlike the case with air-water interface held flat. The goal of this chapter is to grasp the cause of this and thus the influence of the waves on the small scale shear-turbulence (smaller than the LCs) that controls the scalar transfer across the air-water interface via molecular diffusion which is the subject of this chapter.

5.2. Governing Equations and Numerical Setup

In the present chapter, results from the DNS described in the previous chapter are further analysed to assess the importance of the small-scale turbulence (smaller that the Langmuir cells) on scalar transport. Furthermore, large-eddy simulation (LES) will be performed to understand the impact of the wave forcing on the small -scale turbulence as well as the LCs.

The governing equations for the DNS and associated numerical solution technique have been described in previous chapters. The LES consists of the governing equations and numerical

approach described earlier, but with the air-water interface held fixed (flat) and the momentum

equation in (4.1 in chapter 4) for the water side augmented with the Craik-Leibovich (C-L) vortex

force (Craik and Leibovich, 1976) consisting of the cross-product between the Stokes drift velocity

induced by the unresolved air-water interface waves and the flow vorticity:

$$F_i^{CL} = \epsilon_{ijk} u_j^s \omega_k \qquad (5.1)$$

here ϵ_{ijk} is the totally antisymmetric third rank tensor, ω_i is the flow vorticity, and u_j^s is the

inputted Stokes drift velocity. The Stokes drift velocity profile is based on the deep water wave

approximation (Phillips, 1977) with non-zero component in the streamwise (x_1 or x) direction of

the flow (i.e. the wind direction) and zero components in the spanwise (x_2 or y) and vertical (x_3

or z):

$$u_1^s = \left(\frac{2\pi}{\hat{\lambda}}\right)^2 c \exp(-2kz), \ u_2^s = 0, \ u_3^S = 0 \qquad (5.2)$$

where $\hat{\lambda}$ is the wavelength-to-amplitude ratios ($\hat{\lambda} = \lambda/A$) with λ being the dominant wavelength

and A the dominant amplitude of the unresolved surface (air-water interface) waves, $k = 2\pi/\lambda$ is

the dominant wavenumber of the waves , $c = \sqrt{g/k}$ is the phase velocity, z is the distance from

the undisturbed interface (i.e., $z = 0$ at the interface) and g is gravity. Furthermore, in the case of

LES, the advecting velocity in scalar advection-diffusion equation in (4.3), u_j, is reset as $u_j + u_j^s$.

The formulation with the C-L vortex force in the momentum equation in (4.2) and the modified advecting velocity in the scalar advection-diffusion equation in (4.3) in the water side of the domain results from phase-averaging the DNS equations in 4.1-4.2. This procedure averages out the waves occurring at the air-water interface and allows for the simulation to be performed with a flat interface with the effect of wave forcing on the water side accounted for through the vortex force without the need to resolve interfacial waves. Thus, this formulation is referred to as LES. Note that this is not an LES in the traditional sense of spatial filtering described earlier, but rather in the sense of phase-averaging which may be considered as a filter in the time domain. The flow domain, mesh, boundary and initial conditions for the LES follow the same description of Chapter 4 for the DNS.

5.3. Results

For simplicity, flow velocity components will be referred to as u, v and w where $u = u_1, v = u_2$ and $w = u_3$ are the streamwise, spanwise and vertical velocity components, respectively. Similarly $x = x_1, y = x_2$ and $z = x_3$ are the streamwise, spanwise and vertical axis, respectively.

5.3.1. DNS

Following Takagaki et al. (2015), the turbulent structures resolved in the DNS with gravity capillary waves (described earlier in Chapter 4) can also be observed via instantaneous scalar concentration on a spanwise-vertical (y- z) plane at a fixed x, as seen in Figure 5.1. The turbulence is characterized by two principal structures: (1) small-scale LCs which at $t = 6.5$ s occupy the majority of the water side of the domain and (2) smaller surface eddies embedded within the larger LC. The latter are akin to the shear-driven small eddies associated with the classical wall streaks

next to a no-slip wall in turbulent boundary layers (Smith and Metzler, 1983). Initially the Langmuir cells are smaller than those shown in Figure 5.1, and over time grow in depth and spanwise length. By time $t = 6.5$ s, the domain is only able to capture a pair of LCs observed in Figure 5.1. It can be seen that the downwelling limb of the LCs brings high concentration fluid from the surface to depths below, while the upwelling limbs bring low concentration fluid close to the surface.
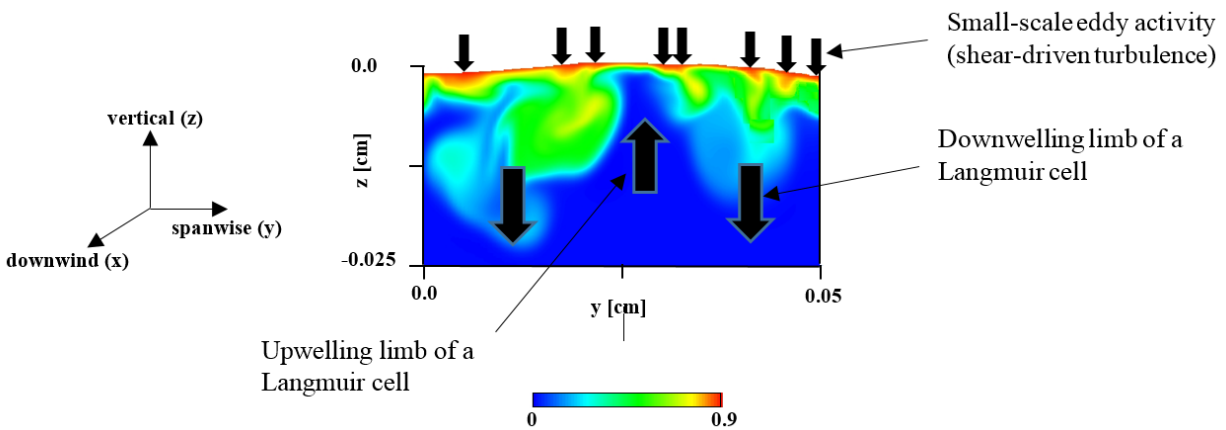

Figure 5.1 Turbulent structures in terms of scalar concentration (mol m^{-3}) in DNS with deformable air-water interface characterized by gravity-capillary waves. The turbulent structures correspond to $t = 6$ s. Downward arrows denote either the downwelling limb of a Langmuir cell or a smaller scale eddy at the surface both bringing high concentration fluid to depths below. The upward arrow corresponds to the upwelling limb of the resolved LCs.

The activity of the smaller shear-driven surface eddies embedded within the LCs can be observed in Figure 5.1 through small filaments of high concentration fluid ejected from the surface within the larger scale vertical scalar transport pattern induced by the downwelling and upwelling limbs of the LCs previously described. The high scalar concentrations carried by these ejections are transported further down by the downwelling limb of the LCs. As noted by Takagaki et al. (2015), these scalar ejections by the smaller eddies serve to thin the molecular diffusive boundary

layer of the scalar, thereby controlling the gradient of scalar across the boundary layer and thus the transfer of scalar across the air-water interface via molecular diffusion.

The distinct scales of the LCs from the rest of the turbulence enable a scale decomposition of the near-surface turbulence to determine the contribution of the LCs to the turbulent vertical flux compared to that of the smaller scale turbulence. In particular, following Takagaki et al. (2015), the near-surface turbulent vertical flux of scalar can be decomposed as:

$$\langle w'C' \rangle \sim \langle w'_{LC} C'_{LC} \rangle + \langle w'_T C'_T \rangle \tag{5.3}$$

where the first term on the right side is the contribution to the flux due to the LCs and the second term is the contribution due to the smaller scale turbulence.

In (5.3), the brackets denote averaging over the streamwise and spanwise directions, and the fluctuations are defined as $w' = w - \langle w \rangle$ and $C' = C - \langle C \rangle$, respectively. Furthermore, the velocity and concentration fluctuations associated with the LCs can be obtained by applying a low pass filter. Specifically, w' and C' at a fixed depth are averaged over the streamwise direction, Fourier transformed in the spanwise direction and low-pass filtered with the spectral cut-off filter (Pope, 2000) with threshold wavenumber of the LCs. The resulting velocity and concentration are then inversed Fourier transformed resulting in w'_{LC} and C'_{LC}. The threshold wavenumber of the LCs is defined as $k_{LC} = 2\pi/D_{LC}$ where D_{LC} is the characteristic spacing of the downwelling limbs of the LCs. Finally, w'_T and C'_T are defined as $w'_T = w' - w'_{LC}$ and $C'_T = C' - C'_{LC}$.

Following the decomposition in (5.3) described above, it can be found that near the surface the contribution of the LCs towards the vertical turbulent flux is relatively small. For example,

at $t = 7$s (after transition to Langmuir turbulence occurs) with $D_{LC} = 0.025$ m, $\langle w'_{LC} C'_{LC} \rangle / \langle w'_T C'_T \rangle = 0.08$ at a depth of 1.5 mm below the unperturbed air-water interface. A similar result led Takagaki et al. (2015) to conclude that in general the near-surface turbulent vertical transport of the scalar is controlled by the smaller scales (i.e. the smaller, shear-driven eddies embedded within the Langmuir cells).

However, in contrast to the previous result in Chapter 4 it was shown that transition to Langmuir turbulence is accompanied by a spike of approximately an order of magnitude in molecular diffusive flux of the scalar across the air-water interface (Figure 4.12 of Chapter 4). Such a spike was noticeably absent in DNS in which the air-water interface is intentionally held flat (i.e. in DNS without LCs) suggesting strong dependence of the flux on LC. As can be also seen in Figure 4.12, after transition to Langmuir turbulence occurs, the DNS exhibits a statistically steady state flux of about 8 times greater than in the DNS with air-water interface held flat, further evidence of the importance of LC towards determining scalar flux. Recall that the molecular diffusive flux of the scalar at the air-water interface is defined as

$$F = \kappa \nabla C \cdot \boldsymbol{n} \tag{5.4}$$

where the gradient of concentration, ∇C, is evaluated at the air-water interface and $\boldsymbol{n}$ is the normal to the interface.

In Chapter 4, the importance of vertical transport induced by LC in determining scalar transfer efficiency was shown in terms of the transfer velocity. The latter is defined as

$$k_L = F / (C_i - C_{bulk}) \tag{5.5}$$

where C_i is the scalar concentration at the air-water interface averaged over the interface and C_{bulk} is the scalar concentration in the bulk of the wind and wave-driven water flow. It was found that the LCs provide intense surface renewal rapidly transporting surface layers and accompanying momentum and scalar to depth from the water surface at rates much larger than that of molecular diffusion and of wind-driven shear turbulence (in the absence of waves). Consequently, in DNS with gravity-capillary waves at the air-water interface (i.e. with LCs), values of $(C_i - C_{bulk})$ are smaller than in DNS with air-water interface held intentionally flat (i.e. with pure wind-driven shear turbulence without LCs). The smaller values of $(C_i - C_{bulk})$ in the DNS with LCs tend to lead to greater k_L. For example, as illustrated in Figure 4.14 in Chapter 4, k_L approximately 8 times greater than k_L values in DNS with interface held flat after transition to Langmuir turbulence had occurred.

5.3.2. LES

Based on the DNS, the decomposition in (5.3) following Takagaki et al. (2015) shows that the contribution of LC to the vertical turbulent flux of scalar near the air-water interface is minor, suggesting that the smaller near-surface eddies are responsible for setting the thickness of the diffusive boundary layer and thus the scalar transfer across the air-water interface via molecular diffusion. However, the role of the wave forcing generating LC remains unclarified given the spike in gas transfer via molecular diffusion during transition to Langmuir turbulence and the subsequent larger values of the diffusive flux compared to DNS without wave forcing in which the air-water interface was held flat (Figure 4.12 in Chapter 4).

In order to reveal the role of wave forcing, LES was performed with the same domain configuration introduced earlier. In the LES, the momentum equation was augmented with the C-

L vortex force described earlier while holding the air-water interface flat. The formulation allows direct input of the Stokes drift velocity facilitating study of the impact of wave forcing on the turbulent structures and ultimately the scalar transfer across the air-water interface via molecular diffusion and the vertical transport of the scalar in the water side. Two LES simulations were performed characterized by different wavelength-to-amplitude ratios ($\hat{\lambda} = \lambda/A$) of the waves generating LC, $\hat{\lambda} = 14$ and $\hat{\lambda} = 25$. The Stokes drift velocity and Stokes drift velocity shear associated with these two values of $\hat{\lambda}$ are shown in Figure (5.2). The Stokes drift shear serves to promote the growth of LC (Holm, 1996), and the LES with $\hat{\lambda} = 25$ is expected to be characterized by more vigorous LC deeper into the water column given its greater Stokes drift shear at depths below the air-water interface.
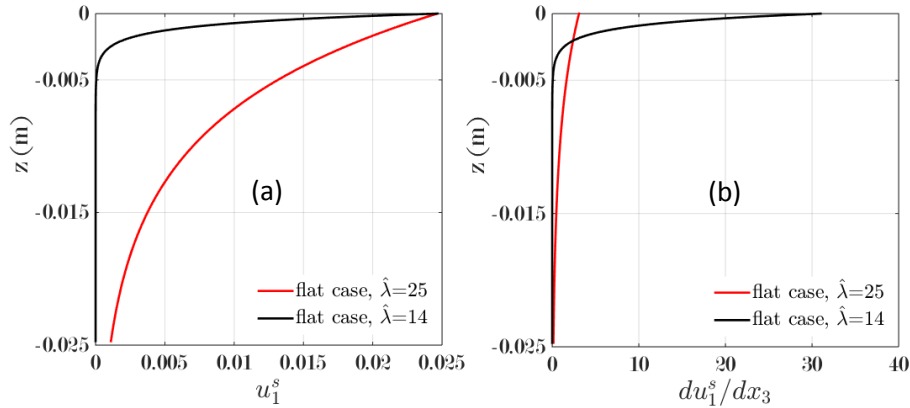

Figure 5.2 (a) Stokes drift velocity and (b) Stokes drift velocity shear in the two LES simulations performed with vortex forcing in water side and air-water face held flat.

Figure 5.3 shows a comparison of downwind-averaged vertical velocity fluctuations at $t = 0.2$ s and 1 s in simulations with interface held flat with and without C-L vortex forcing. These fluctuations reveal the downwelling and upwelling limbs of the turbulent eddies resolved.

The simulation without C-L vortex forcing is driven purely by the air flow above the air-water interface. In this case shown in panels (a)-(c) of Figure 5.3, the near-surface eddies are shear-driven and are akin to the shear-driven eddies associated with the classical wall streaks next to a no-slip wall in turbulent flow (Smith and Metzler, 1983). Note that the surface shear-driven eddies remain present in the flows with C-L vortex forcing (panels (d)-(i)) while now embedded within the larger LCs in similar fashion to how they were observed in DNS with gravity-capillary waves at the air-water interface (Figure 5.1). The LCs quickly grow in depth and spanwise length, and eventually by time $t = 1$ s (panels (e) and (f) of Fig. 5.3), a single pair occupies the entire spanwise extent of the domain in both cases with $\hat{\lambda} = 14$ and $\hat{\lambda} = 25$. This is also consistent with the DNS. As expected, the LCs obtained with Stokes drift with $\hat{\lambda} = 25$ in the C-L vortex force penetrate deeper in the water column than the LCs obtained with $\hat{\lambda} = 14$. This can be observed by comparing the LCs at $t = 1$ s in panels (e) and (f) and is due to the greater Stokes drift shear reaching deeper in the water column in the case with $\hat{\lambda} = 25$ (Figure 5.2).

Remarkably, the Stokes drift shear not only serves to promote the growth of LCs but also is seen to strengthen the near-surface smaller eddies. This can be observed by comparing panel (c) in Figure 5.3 (LES without C-L vortex forcing) with panels (f) and (i) (LES with C-L vortex forcing). In the cases with C-L vortex forcing, the Stokes drift shear leads to more intense small eddies compared to the case without the vortex force. Furthermore, the small eddies in the flow with $\hat{\lambda} = 14$ are of greater intensity than the eddies in the flow with $\hat{\lambda} = 25$, seen by comparing panels (f) and (i) in Figure 5.3. This is attributed to the greater near-surface Stokes drift shear in the $\hat{\lambda} = 14$ case, seen in Figure 5.2. In turn, the stronger near-surface small eddies in the flow with $\hat{\lambda} = 14$ lead to greater diffusive flux of the scalar across the air-water interface, seen in Figure 5.4.

In both flows with C-L vortex forcing, the transition to Langmuir turbulence leads to a spike in scalar flux across the interface, whereas this spike is absent in the case without the vortex forcing (Figure 5.4), consistent with the DNS results in Figure 4.12 of Chapter 4. Although the small eddies control the scalar transfer across the interface as originally concluded by Takagaki et al. (2015), the presence of the waves and thus Langmuir forcing significantly enhances the scalar transfer induced by the small eddies.
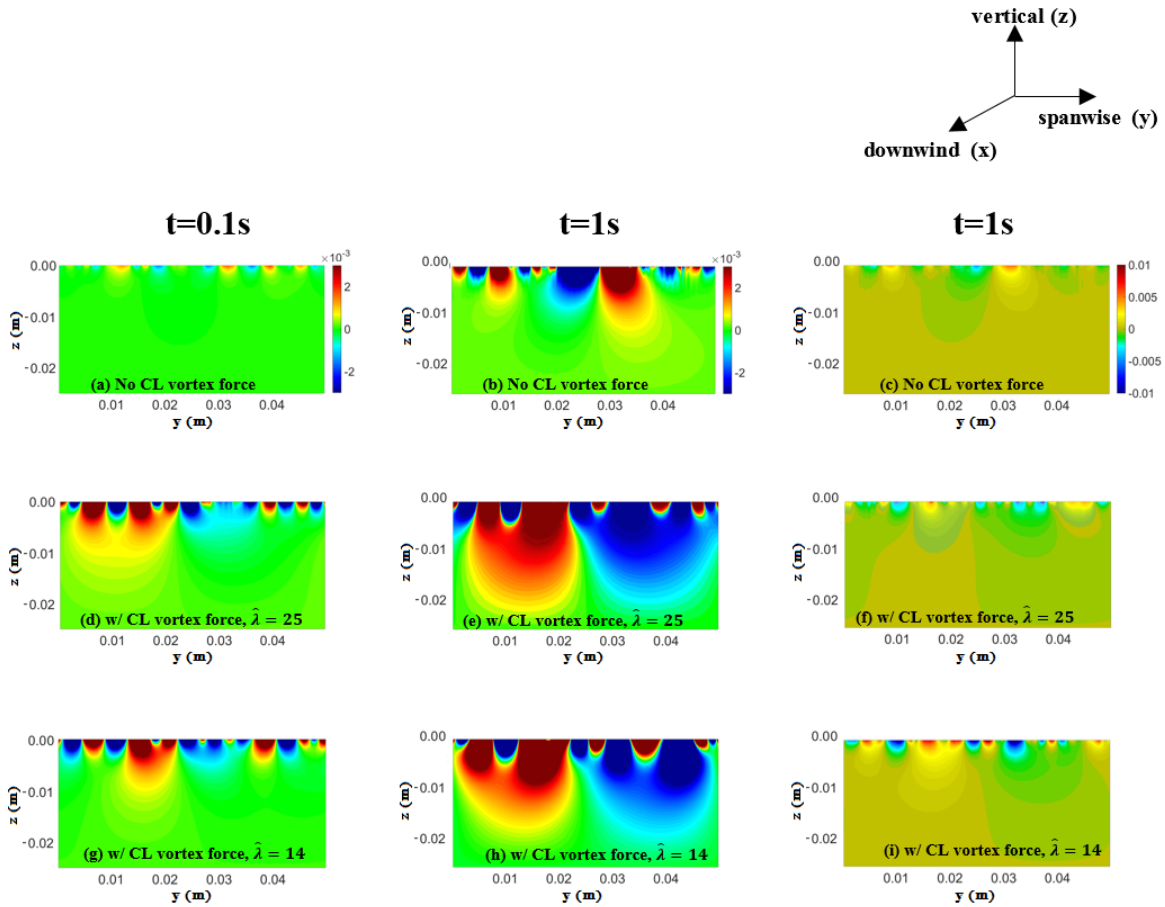

Figure 5.3 Downwind-averaged vertical velocity fluctuations, w', at t = 0.1 and 1 s over the spanwise-vertical extent of the domain in simulations with interface held flat with and without CL vortex forcing (i.e. with and without LCs). In LES with CL vortex force, the Stoke drift was set with either $\hat{\lambda}$ = 14 or $\hat{\lambda}$ = 25. Panels (c), (f) and (i) presents the same data as panels (b), (e) and (h) but with different scale in order to better highlight the intensity of the near-surface small eddies.
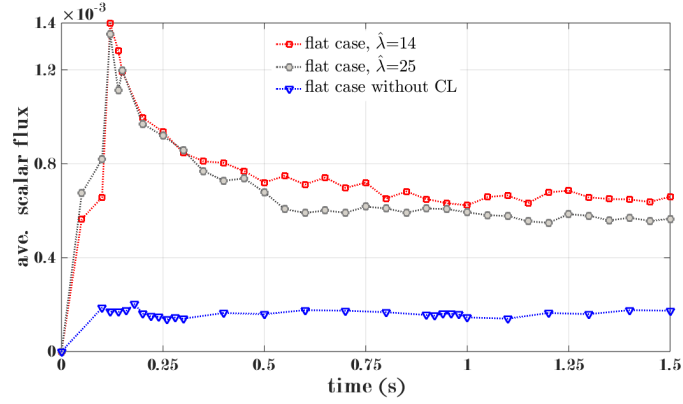
Figure 5.4 Molecular diffusive flux of the scalar at the air-water interface in simulations with flat interface with or without CL vortex forcing. The simulations with vortex forcing are characterized by the value of $\hat{\lambda}$ in the Stokes drift velocity. The fluxes were averaged over the interface.

To investigate the impact of the turbulent scales (i.e., the LC and the smaller eddies) on vertical turbulent flux of the scalar, the vertical velocity and concentration fluctuations are decomposed following the low pass filtering approach originally proposed by Takagaki et al. (2015) described earlier in sub-section 5.3.1. As noted earlier, by $t = 1$s a pair of LCs occupies the entire spanwise extent of the domain (see panels (e) and (h) in Fig. 5.3), hence the spanwise spacing of the downwelling limbs of the LCs is taken as $D_{LC} = 0.05$ m, corresponding to the spanwise length of the domain. Thus the cut-off wavenumber in the spanwise low pass filtering of the velocity and concentration fluctuations (w' and C', respectively) is $k_{LC} = 2\pi/D_{LC} = 125.6$ m^{-1}. Recall that this low pass filtering operation decomposes a field as $f = f_{LC} + f_T$ where f_{LC} is the low pass filtered field associated with the LC and f_T is the residual associated with the smaller scale turbulence (smaller than the LC). The low-pass filtered velocity and concentration fluctuations, w'_{LC} and C'_{LC}, are plotted in Figure 5.5 along with their unfiltered counterparts, w' and C', for the flows with vortex forcing at $t = 1$ s and at depth 1.5 mm from the air-water interface.

It can be seen that the contributions of the LC to the vertical velocity and scalar concentration fluctuations are relatively small, as would be expected given that the small eddies are active close to the surface (i.e. at 1.5 mm below the air-water interface).
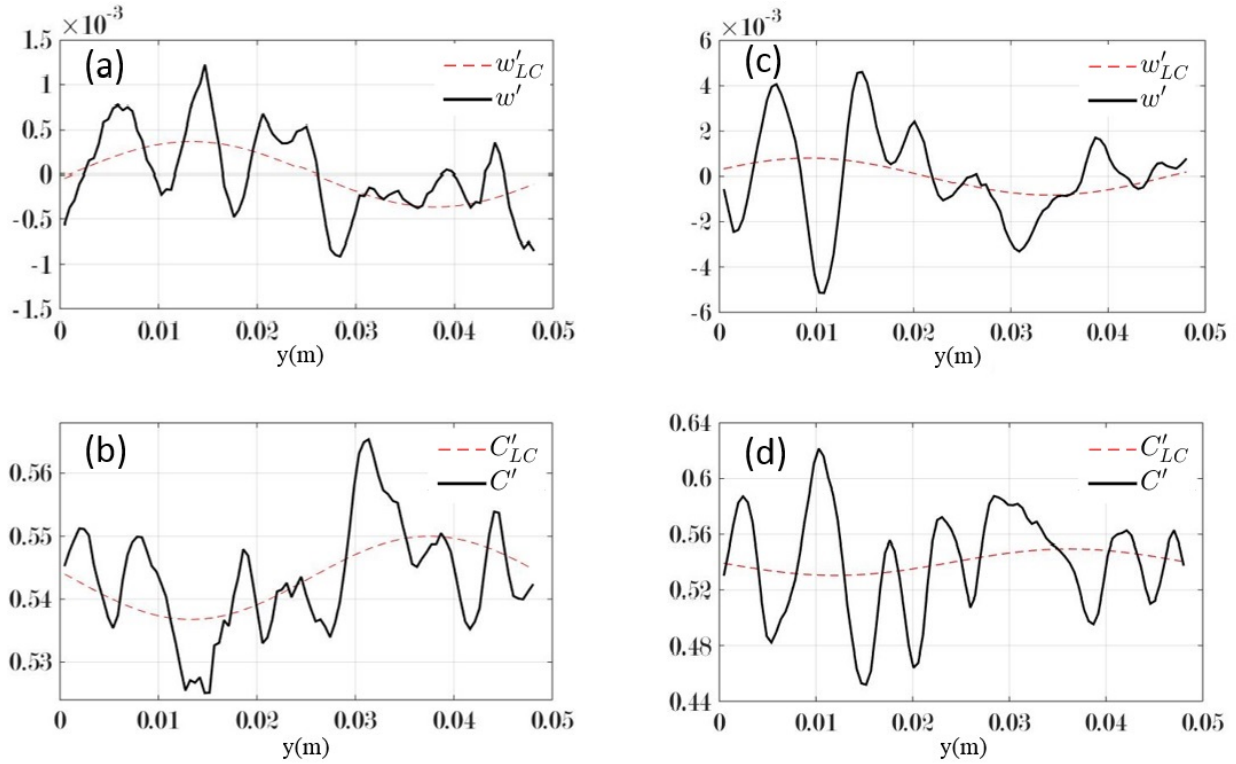

Figure 5.5 Downwind-averaged, low-pass filtered and unfiltered velocity (w'_{LC} and w', respectively) and scalar concentration (C'_{LC} and C', respectively) fluctuations plotted vs. spanwise direction at 1.6 mm from the air-water interface in flows with LC with $\hat{\lambda} = 25$ in the vortex force ((a) and (b)) and with $\hat{\lambda} = 14$ ((c) and (d)).

The importance of LC relative to the smaller scale turbulence in determining the vertical turbulent flux of the scalar may be measured through the ratio $\langle w'_{LC} C'_{LC} \rangle / \langle w'_T C'_T \rangle$. At 1.5 mm depth below the surface, this ratio is 0.079 and 0.155 for the flows with $\hat{\lambda} = 14$ and $\hat{\lambda} = 25$, respectively. Thus in both cases, the contribution of the LCs to the overall vertical turbulent flux of the scalar is

relatively small compared to the contribution from the smaller scales, as would be expected given the presence of the dominant small eddies near the surface. This is the same conclusion obtained from the DNS of Takagaki et al. (2015) and our own DNS both reviewed earlier. In order to further investigate the LC contribution, the quantity $\langle w'_{LC} C'_{LC} \rangle / \langle w'_T C'_T \rangle$ is plotted as a function of depth in Figure 5.6. Here it can be observed that the contribution of LC to $\langle w'C' \rangle$ increases away from the air-water interface as would be expected, given that the smaller eddies occupy the near-surface region whereas the LC extends deeper into the water column. This behaviour is observed in both the LC cases with C-L vortex forcing and in the DNS.

The above analysis paints an effective system for the vertical turbulent transport of the scalar in which near the surface the small eddies are directly enhanced by the Stokes drift shear providing the dominant mechanism in vertical transport. Meanwhile deeper in the water column, the Stokes drift shear generates vigorous LC serving to carry the scalar to greater depths than in flow with shear-driven near-surface small eddies only (without C-L vortex forcing).
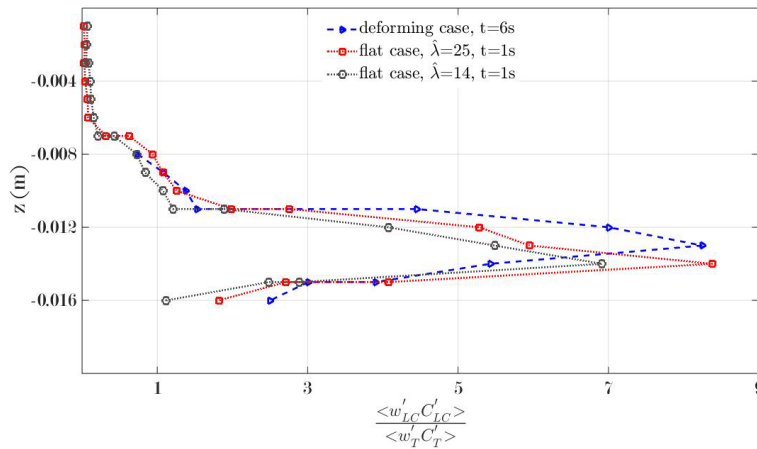

Figure 5.6 LC contribution to the vertical turbulent flux of the scalar in flows with LC and C-L vortex forcing (flat cases) and in the DNS (deforming case) with or without CL vortex forcing. The simulations with vortex forcing are characterized by the value of $\hat{\lambda}$ in the Stokes drift velocity. The fluxes were averaged over the streamwise and downwind directions.

5.3.3. Chapter Summary

In Chapter 4, it was revealed that the presence of the near surface eddies by themselves in the DNS with air-water interface held intentionally flat led to lower values of the scalar flux across the interface than that of the DNS with waves (deforming case). In this Chapter, multiple LES scenarios with different C-L vortex forcing were performed using the same configuration as the DNS, but with the air-water interface held flat to investigate the effect of waves and thus the Stokes drift shear on the small, shear-driven eddies at the surface. It was observed that these eddies control the scalar transfer across the air-water interface while the presence of Stokes drift shear intensifies these small eddies leading to the spike in scalar transfer during transition to Langmuir turbulence as well as to an overall greater scalar flux relative to flow without the C-L vortex force (i.e. without wave forcing). Moreover, the wave-induced LC also leads to enhanced vertical transport of the scalar at greater depths than those reached by the shear-driven small eddies thereby increasing transfer efficiency throughout the water column.

CHAPTER 6: CONCLUSIONS AND FUTURE RESEARCH

In this dissertation several DNS and LES scenarios of a wind driven air-water interface characterized by gravity-capillary waves and molecular sublayers below and above the interface have been performed to better understand the impact of the waterside turbulence on scalar transfer from the air side to the water side and subsequent vertical transport in the water column. The flow generated gravity-capillary waves along the air-water interface which combined with the aqueous shear flow led to development of small-scale (centimeter-scale) LC. Results from the DNS simulations showed that vertical transport induced by the LCs enhances bulk concentration throughout the water column which ultimately enhances transfer velocity, a measure of scalar transfer efficiency. The DNS also revealed that the spike in scalar transfer across the air-water interface occurred in the presence of waves only as a DNS in which the air-water interface was held flat (thereby precluding the LC but not shear-driven small eddies) did not yield a similar spike. LCs rapidly transport surface layers to depth thereby transporting momentum and scalars away from the surface at rates much larger than shear-driven turbulence occurring when the air-water interface was intentionally held flat.

Moreover, transition to Langmuir turbulence was observed to be accompanied by a spike in scalar flux characterized by an order of magnitude increase. These episodic flux increases, if linked to gusts and unsteadiness in the wind field, are expected to be an important contributor in determining the long-term average of the air-sea fluxes. The spike in scalar flux occurred during

transition to turbulence while the mean far-field wind speed was constant, thus the wind speed would not be able to serve as a proxy for the spike in transfer velocity.

In Chapter 5, it was revealed that, in addition to LC, the turbulence is characterized by near-surface eddies of smaller size and embedded within the LC. The observed eddies were attributed to the shear on the water side and not the waves, as these eddies are akin to the shear-driven eddies associated with the classical wall streaks next to a no-slip wall in turbulent boundary layers (Smith and Metzler, 1983). A scale decomposition performed allowed to determine the contribution of the LCs to vertical turbulent flux of the scalar relative to the contribution of the smaller scale turbulence, showing that the small, shear-driven eddies were the dominant drivers of scalar transfer from the air side to water side and not the LC. Furthermore, the presence of the near surface eddies by themselves in the DNS with air-water interface held intentionally flat led to lower values of the scalar flux across the interface, relative to the DNS with waves.

LES was performed using the same configuration as the DNS, but with the air-water interface held flat to clarify the effect of waves and thus the Stokes drift shear on the scalar flux across the interface. It was observed that the presence of Stokes drift shear intensifies the small shear-driven eddies leading to the spike in scalar transfer during transition to Langmuir turbulence as well as to an overall greater scalar flux relative to flow without the C-L vortex force (i.e. without wave forcing). Meanwhile the wave-induced LC leads to enhanced vertical transport of the scalar at greater depths than those reached by the shear-driven small eddies thereby increasing transfer efficiency throughout the water column.

In the last decades, the world has witnessed an alarming and costly impact from Global warming which threatens our societies' health and existence. For these reasons scientists have been more focused on exchange of greenhouse gases between the atmosphere and the oceans. Due to

the increase in computation capabilities, as an alternative to experimental data which has proven to be difficult to acquire, DNS is now becoming a key tool that will help develop more effective parameterizations of gas transfer velocity needed by climate models to predict gas fluxes into the ocean. The DNS via the OpenFOAM methodology used in this study is found to replicate oceanic turbulence and its physical impact on gas uptake as perceived through experiment, which is an indicator that it can be adopted to improve the gas transfer velocity models needed for global climate modelling.

Future research should exploit DNS and LES in order to enhance parameterizations of the scalar transfer velocity (a measure of transfer efficiency) through the incorporation of Stokes drift shear dependence. Additionally, future work should explore the wind speed dependence on intermittent and intense enhancement in scalar transfer occurring during rapid transition to turbulence in the presence of waves. In the field, these spikes are expected to occur frequently associated with wind gusts, and thus may account for the bulk of gas transfer in the gravity-capillary wave regime.

REFERENCES

Baehr, H. D., Stephan, K., 2006. Heat and Mass Transfer. Springer.

Banerjee, S., Scott, D.S., Rhodes, E., 1968. Mass transfer to falling wavy liquid films in turbulent flow, Ind. Eng. Chem. Fundamentals **7**, 22–27.

Banerjee, S., Lakehal, D. and M. Fulgosi., 2004. Surface divergence models for scalar exchange between turbulent streams. Int. J. Multiphase Flow, 30(30):963–977.

Banerjee, S., 2007. Modeling of interphase turbulent transport processes. Ind. Eng. Chem. Res. 46, 3063–3068.

Coles, D., 1956. The law of the wake in the turbulent boundary layer. J. Fluid Mech. 1, 191.

Courant, R., Friedrichs, K., Lewy, H., 1967. On the partial difference equations of mathematical physics," IBM J. Res. Develop., 11 (), pp. 215–234.

Craik, A.D.D., and Leibovich, S., 1976. A rational model for Langmuir circulations. J. Fluid Mech. 73, 401–426.

Danckwerts, P.V., 1951. Significance of liquid-film coefficients in gas absorption. Ind. Eng. Chem., 43:1460–1467.

Deshpande, S.S., Anumolu, L., Trujillo, M.F., 2012. Evaluating the performance of the two-phase flow solver interFoam, Comput. Sci. Discovery, 5, Article 014016.

Donelan, M.A., 1998. Physical Processes in Lakes and Oceans, in: Imberger, J. (Ed.), Coastal and Estuarine Studies. American Geophysical Union, Washington, D. C., pp. 1–668.

EPA. "Overview of Greenhouse Gases: Carbon dioxide emissions". http://www.epa.gov/climatechange/ghgemissions/gases/co2.html .

Frew, N.M., Bock, E.J., Schimpf, U., Hara, T., Haußecker, H., Edson, J.B., McGillis, W.R., Nelson, R.K., McKenna, S.P., Uz, B.M., J¨ahne, B., 2004. Air-sea gas transfer: Its dependence on wind stress, small-scale roughness, and surface films. J. Geophys. Res., 109, C08S17, doi:10.1029/2003JC002131.

Harlow, F.H., Welch, J.E., 1965. Numerical Calculation of Time-Dependent Viscous Incompressible Flow of Fluid with Free Surface. Physics of Fluids (1958-1988), 8, 2182-2189. http://dx.doi.org/10.1063/1.1761178

Higbie, R., 1935. The rate of absorption of a pure gas into a still liquid during a short time of exposure. Trans. Am. Inst. Chem. Eng., 31:365–389.

Hirt, C.W., Nichols, B.D., 1981. Volume of Fluid (VOF) Method for the Dynamics of Free Boundaries, Journal of Computational Physics. 39, 201-225.

Holm, D., 1996. The ideal Craik-Leibovich equations. Phys. D Nonlinear Phenom. 98, 415–441.

Hung, L., Tsai, W., 2007. A Numerical Study on the Characteristic Flow Structures of a Micro-Breaking Wind Wave. Chapter: The Air-Water Interface: Turbulence and Scalar Exchange, pages 159-168. Springer.

Iwano, H., Orihashi, Y., Hirata, T., 2013. An inter-laboratory evaluation of OD-3 zircon for use as a secondary U–Pb dating standard. Island Arc 22,doi:10.1111/iar.12038.

Kader, B.A., Yaglom, A.M., 1972. Heat and mass transfer laws for fully turbulent wall flows, J. Heat Mass Transfer **15**, 2329-2353.

Komori, S., Nagaosa, R., Murakami, Y., 1993. Turbulence structure and mass transfer across a sheared air-water interface in wind-driven turbulence. J. Fluid. Mech. 249, 161_183.

Komori, S., Kurose, R., Iwano, K., Ukai, T., Suzuki, N., 2010. Direct numerical simulation of wind-driven turbulence and scalar transfer at sheared gas–liquid interfaces. Journal of Turbulence, 11, N32, doi:10.1080/14685248.2010.499128.

Lamb, H., 1932. Hydrodynamics (Cambridge: Cambridge University Press), page 445.

Lewis, W.K., Whitman, W., 1924. Principles of gas absorbtion. Ind. Eng. Chem., 16:1215 U 1224.

Liss, P.S., Merlivat, L., 1986. Air-sea gas exchange rates: Introduction and synthesis, In The Role of Air-Sea Exchange in Geochemical Cycling, edited by P.Buat-Menard, 113-129, D. Reidel, Norwell, Mass.

MacIntyre, S., Alldredge, A.L., Gotschalk, C.J., 1995. Accumulation of marines now at density discontinuities in the water column. Limnography and Oceanography, 113,10.4319/lo.1995.40.3.0449

Márquez, D.S., 2013. An Extended Mixture Model for the Simultaneous Treatment of Short and Long Scale Interfaces. Ph.D. thesis, Facultad de Ingenieria y Ciencias Hidricas, Universidad Nacional del Litoral.

McCready, M.J., Vassiliadou, E., Hanratty, T.J., 1986. Computer simulation of turbulent mass transfer at a mobile interface, AIChE J. **32(7)**, 1108–1115.

Nagaosa, R., Handler, R., 2012. Characteristic Time Scales for Predicting the Scalar Flux at a Free Surface in Turbulent Open-Channel Flows. AIChE J, 58: 3867–3877, doi: 10.1002/aic.13773.

Nightingale, P.D.G., Malin, C.S., Law, A.J., Watson, P.S., Liss, M.I., Liddicoat, J., Boutin, Upstill-Goddard, R.C., 2000. In-situ evaluation of airseagas exchange parameterisations using novel conservative and volatile tracers, Global Biogeochem. Cycles, 14, 373 – 387, 2000.

OpenCFD, OpenFOAM, 2002. The Open Source CFD Toolbox, User Guide. OpenCFD Ltd.

Patankar, S.V., Spalding, D.B., 1972. A Calculation Procedure for Heat, Mass and Momentum Transfer in Three-dimensional Parabolic Flows, Int. Journal of Heat Mass Transfer. **15**, 1787.

Phillips, O.M., 1977. The Dynamics of the Upper Ocean. Cambridge University Press, 336 pp.

Pope, S.B., 2000. Turbulent Flows. Cambridge University Press.

Prosperetti, A., 1981. Motion of two superposed viscous fluids. Physics of Fluids (1958-1988). 24(7). 1217–1223.

Sahay, K.R., Sreenivasan, 1999. The wall-normal position in pipe and channel flows at which viscous and turbulent shear stresses are equal. Physics of Fluids, 11:3186-3188.

Schlichting, H., 1960. Boundary layer theory, McGraw-Hill. McGraw-Hill.

Smith, C.R., Metzler, S.P., 1983. The characteristics of low-speed streaks in the near-wall region of a turbulent boundary layer J. Fluid Mech. 129, 21-54.

Suzuki, N., Donelan, M., Komori, S., Takagaki, N., 2015. Estimation of the global air-sea CO2 gas flux considering wave breaking. Journal of Oceanography.

Takagaki, N., Kurose, R., Tsujimoto, Y., Komori, S., Takahashi, K., 2015. Effects of turbulent eddies and Langmuir circulations on scalar transfer in a sheared wind-driven liquid flow, Phys. Fluids 27, 016603.

Tejada-Martínez, A.E., 2002. Dynamic Subgrid-Scale Modeling for Large-Eddy Simulation of Turbulent Flows with a Stabilized Finite Element Method. Rensselaer Polytechnic Institute.

Tennekes, H., Lumley, J.L., 1972. A First Course in Turbulence. Massachusetts Institute of Technology, Cambridge.

Thorpe, S.A., 2004. Langmuir circulation, Annu. Rev. Fluid Mech. **36**, 55.

Toor, H. L., Marchello, J.M., 1958. Film-penetration model for mass and heat transfer. A.I.Ch.E. Journal, 4, 97.

Tsai, W., Chen, S., Lu, G., 2013. Characteristics of interfacial signatures on a win-driven gravity-capillary wave. J. Geophy. Res. Oceans, 118, 1715-1735, doi:10.1002/jgrc.20145.

Veron, F., Melville, W.K., 2001. Experiments on the stability and transition of wind driven water surfaces, J. Fluid. Mech. **446**, 25-65.

Wanninkhof, R., 1992. Relationship between wind speed and gas exchange over the ocean, J. Geophys. Res. **97**, 7373–7382.

Wanninkhof, R., McGillis, W.R., 1999. A cubic relationship between air-sea CO2 exchange and wind speed, Geophysical Research Letters, 26, 1889

Wanninkhof, R., Donelan, M.A., 2002. Gas Transfer at Water Surfaces: Concepts and Issues, volume 127. Geophys. Monogr. Ser., AGU, Washington, D. C.

Wanninkhof, R., Asher, W.E., Ho, D.T., Sweeney, C.S., McGillis, W.R., 2009. Advances in quantifying air-sea gas exchange and environmental forcing. Annu. Rev. Mar. Sci., 1:213–244.

Wardle , K.E., Allen , T.R., Anderson , M.H., Swaney, R.E., 2008. Free surface flow in the mixing zone of an annular centrifugal contactor. AIChE J., 54:74.

Woolf, D.K., 2005. Parametrization of gas transfer velocities and sea-state-dependent wave breaking. Tellus B. 57, 8794.

Zappa, C.J., McGillis, W.R., Raymond, P.A., Edson, J.B., Hintsa, E.J., Zemmelink, H.J., Dacy, J.W. and Ho., D.T., 2007. Environmental turbulent mixing controls on air-water gas exchange in marine and aquatic systems. Geophys. Res. Lett. **34**, L10601.

Zhao, D., Toba, Y., Sugioka, K., Komori, S., 2006. New sea spray generation function for spume droplets. J. Geophys. Res. 111, C02007. DOI: 10.1029/2005JC002960.

APPENDIX A: VALIDATION

One of the validation problems simulated has been that of a two-dimensional standing capillary wave. Here an air-water interface is perturbed as shown in Figure A.1 and allowed to return to its unperturbed state under the influence of surface tension only (excluding gravity). The interface returns to its unperturbed state while exhibiting an exponentially decaying temporal oscillation. For a sufficiently small initial perturbation amplitude, the decaying oscillation frequency has been obtained analytically by Lamb (1932). The frequency of interface oscillation ω_{osc} is given as

$$\omega_{osc} = \sqrt{\frac{\sigma k^3}{\rho_{water} + \rho_{air}}} \qquad\qquad (A.1)$$

where:

σ is the air-water surface tension in N/m.

λ is the wavelength in m.

$k = \frac{2\pi}{\lambda}$ is the wavenumber in m^{-1}.

ρ_{water} is the water density in kg/m^3.

ρ_{air} is the air density in kg/m^3.

Furthermore, the rate of decay of global vertical kinetic energy (KE) of the water due to both viscosity, v_{water}, and surface tension, σ, was also solved analytically by Lamb.

The dimensionless solution is given below:

$$KE(t)/KE_{max} = e^{-4v^*t^*} \tag{A.2a}$$

$$t^* = \frac{t}{\sqrt{\rho_{water}/(\sigma k^3)}} \tag{A.2b}$$

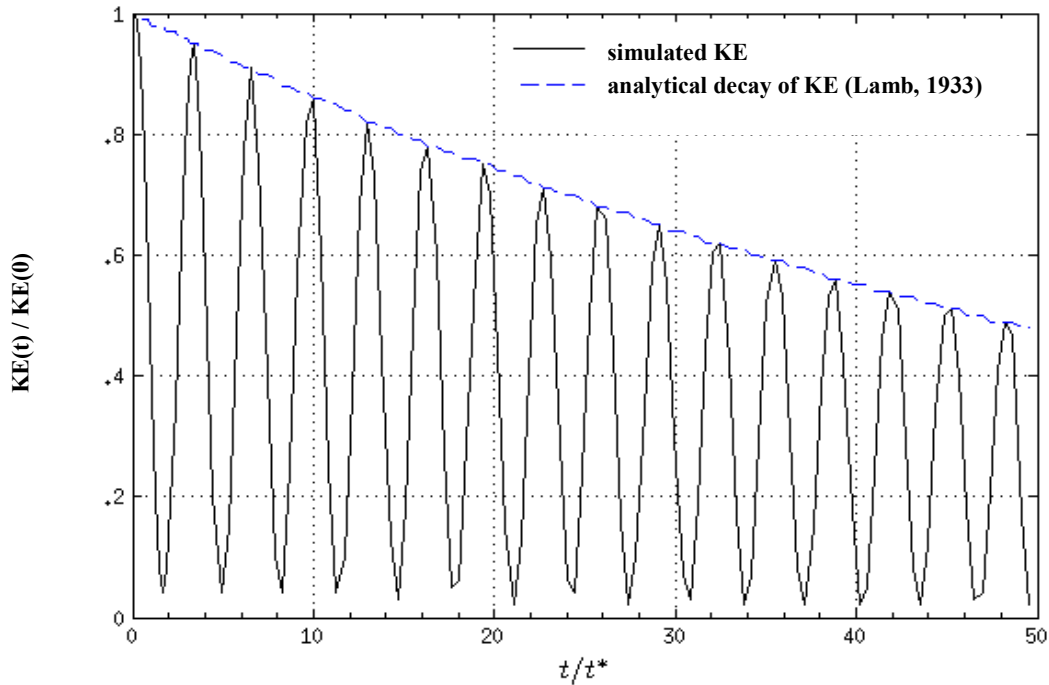$$v^* = v_{water} \, k^2 \, \sqrt{\rho_{water}/(\sigma k^3)} \tag{A.2c}$$
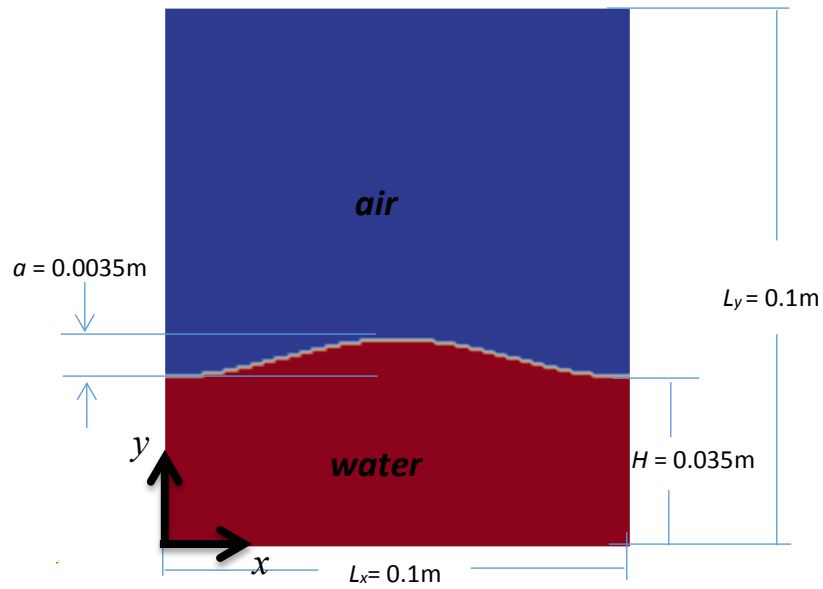
Figure A.1 Time series of global vertical kinetic energy (KE) of water normalized by its maximum value and time series of analytically-determined decay of Lamb (1932).

The simulation is initialized with a perturbation of the air-water interface with a wavelength of $\lambda = 0.1$ m and an amplitude $a = H/10$ (see Figure A.1) where $H = 0.035$ m is the depth of the

unperturbed water. This initial perturbation is allowed to decay in time under the influence of surface tension.

The densities of water and air were set to 1000 kg/m³ and 1.204819 kg/m³ respectively, the air water surface tension was set to 0.07286 N/m and the kinematic viscosity of water and air were set to $1.0 * 10^{-6} \ m^2/s$ and $1.5 * 10^{-5} \ m^2/s$ respectively.

A structured mesh of 200 hexahedral elements along x and 180 hexahedral elements along y was used for the simulation. The lateral boundary conditions were chosen as periodic along with a no-slip condition at the bottom of the water column.

Figure A.2 Time series of global vertical kinetic energy (KE) of water normalized by its maximum value and time series of analytically-determined decay of Lamb (1932).

The simulation is characterized by the temporal oscillatory decay of the interfacial wave, manifested through a decaying global vertical kinetic energy of the water defined as

$$KE(t) = \int_{\Omega_{water}} w \, dxdy \qquad (A.3)$$

where Ω_{water} is the volume of the water and w is the vertical velocity of the water. Figure A.2 shows the time evolution of the global vertical kinetic energy normalized by its maximum value. Its overall decay is in good agreement with the analytically-derived decay of Lamb (1932). Furthermore, the frequency of oscillation computed as 8.5 Hz is also in good agreement with Lamb's analytical solution.

Lastly, Prosperetti (1981) derived an analytical solution for the same problem studied here, when both surface tension and gravity are considered. Recall that the solutions previously described excluded the effect of gravity. With the inclusion of gravity the frequency of decaying wave oscillation was obtained analytically by Prosperetti (1981) as

$$\omega_{osc} = \sqrt{\frac{\sigma * k^3}{(\rho_{water} + \rho_{air})} + \frac{(\rho_{water} - \rho_{air})}{(\rho_{water} + \rho_{air})} gk} \qquad (A.4)$$

Simulations with the inclusion of gravity (not shown) have been found to be in good agreement with Prosperetti's analytical solution.

APPENDIX B: TURBULENT BOUNDARY LAYER

Unlike in laminar boundary layers where fluid flows occur similar to sliding laminates or laminates, turbulent boundary layers are characterized by intense agitation and eddy mixing across many layers simultaneously, resulting in a much more effective mixing of energy, momentum and mass across the water column.

In 1904, Ludwig Prandtl was the first who introduced the concept of boundary layer. Prandtl established that, for any viscous fluid that flows over a stationary solid body, the fluid slows down due to frictional forces resisting its flow while two distinct regions are observed. The first region is the boundary layer characterized by viscosity dominance on the flow while the second region is characterized by minimal viscosity control and thus may be considered nearly inviscid (Figure B.1).
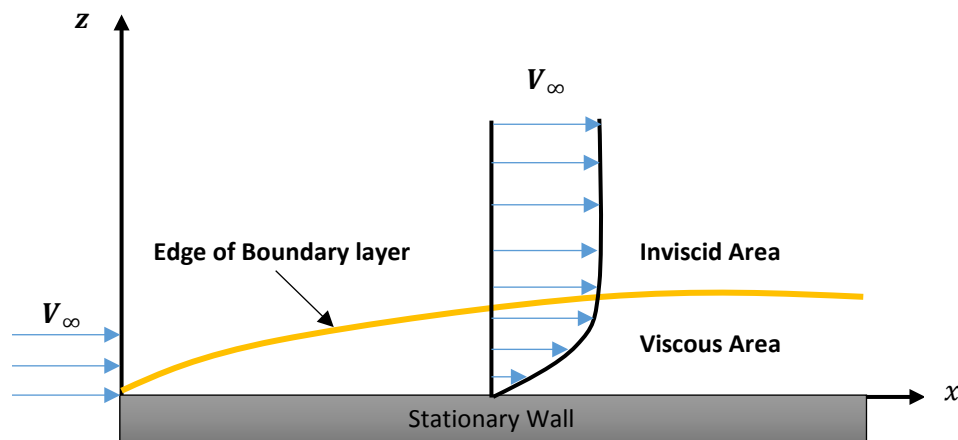
Figure B.1 Turbulent boundary layer structure

Prandtl established a mixing length 'l' which he defined as the distance for which an eddy is retaining its identity before collision with other eddies. This theory is an analogy to the theory of mean free path in Thermodynamics. Moreover, Prandtl proposed that the mixing length is proportional to the normal distance between the wall boundary and the eddy as follows:

$$l = \kappa * y \tag{B.1}$$

where κ is the empirical Von Karman's constant ($\kappa = 0.41$) and y is the wall-normal distance from the wall.
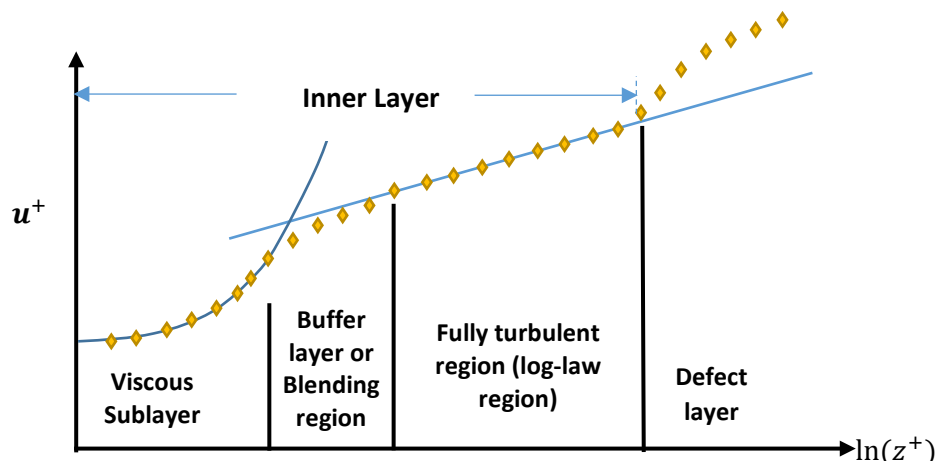
Figure B.2 Turbulent boundary layer structure

The near-wall region may be subdivided into four different regions as suggested in Figure B.2. These four regions will be described in more detail below.

- The viscous sub-layer is the nearest region to the wall, where molecular viscosity is predominant in momentum transport while turbulence is negligible. This layers covers

(normalized) wall distances in the range $0 < z^+ < 5$ (Tennekes et. al, 1972), where z^+ is the dimensionless wall distance in wall units $z^+ = \frac{u_\tau z}{v}$ where v is the dynamic viscosity. Within the viscous sub-layer, mean streamwise velocity u^+ can be approximated as

$$u^+ = z^+ \tag{B.2}$$

where $u^+ = \frac{u}{u_\tau}$ is the mean streamwise velocity scaled by wall friction velocity $u_\tau = \sqrt{\tau_w / \rho}$ which depends on the wall shear stress τ_w and the density ρ.

The buffer layer or blending region is where both turbulence and molecular viscosity are important in momentum transport and in particular, maximum turbulence production occurs at approximately $z^+ = 12$, according to Sahay and Sreenivasan (1999). This region occurs for (normalized) distances from the wall in the range $5 < z^+ < 3$ (Tennekes et al., 1972).

- The inertial sub-layer or the log-layer is where turbulence is predominant in momentum transport while viscous effects are negligible. This region is observed for (normalized) wall distances such as $30 < z^+ < 200$ (Tennekes et. al, 1972), where the (normalized) mean streamwise velocity u^+ is observed to be following a logarithmic correlation given as follows:

$$u^+ = \frac{1}{\kappa} * \ln(z^+) + B \tag{B.3}$$

where the Van Karman coefficient is approximated as $\kappa = 0.4$ is and the coefficient $B \approx$ 5.5 (Schlichting, 1960)

- The defect layer or the outer layer is where the mean streamwise velocity can be approximated by the Law of the Wake established by Coles (1956) as
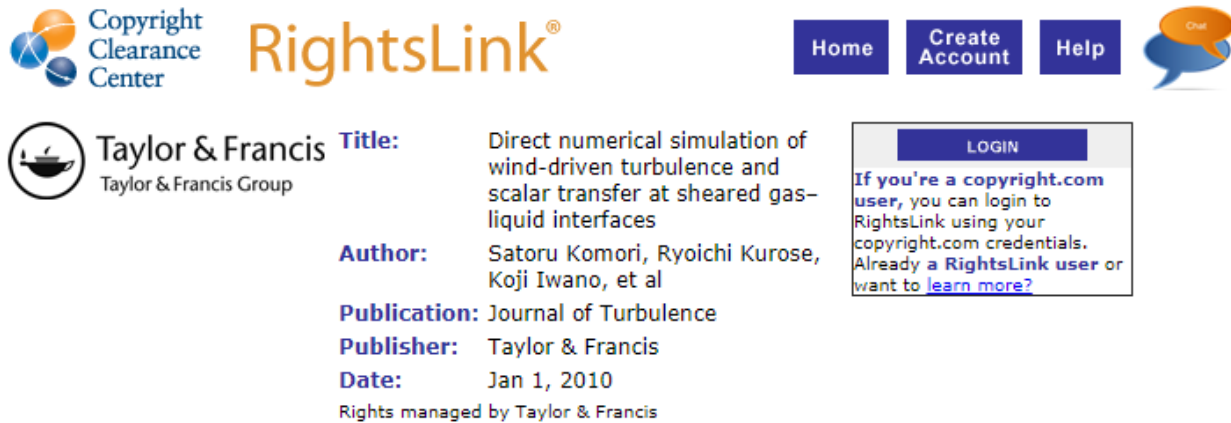
$$u^+ = \left(\frac{1}{\kappa} * \ln(z^+) + B\right) + \Pi(z^+) \tag{B.4}$$

where Π is an empirical wake function that depends on the Reynolds number.

APPENDIX C: RIGHTS AND PERMISSIONS

C.1 Permissions to Use the Figures in Chapter 1

C.1.1 Permission to Use Figure 1.3

Copyright Clearance Center · RightsLink®

Home | Create Account | Help

Taylor & Francis
Taylor & Francis Group

Title: Direct numerical simulation of wind-driven turbulence and scalar transfer at sheared gas–liquid interfaces

Author: Satoru Komori, Ryoichi Kurose, Koji Iwano, et al

Publication: Journal of Turbulence

Publisher: Taylor & Francis

Date: Jan 1, 2010

Rights managed by Taylor & Francis

LOGIN

If you're a copyright.com user, you can login to RightsLink using your copyright.com credentials. Already a RightsLink user or want to learn more?

Thesis/Dissertation Reuse Request

Taylor & Francis is pleased to offer reuses of its content for a thesis or dissertation free of charge contingent on resubmission of permission request if work is published.

BACK | CLOSE WINDOW

C.2 Permissions to Use the Figures in Chapter 2

C.2.1 Permission to Use Figure 2.1

Tejada-Martinez, Andres ▬▬▬▬▬▬   3:34 PM (42 minutes ago)
to me

Yes, please use it.

Andres

Amine Hafsi <ahafsi@mail.usf.edu>
to Andres

Dear Dr. Tejada-Martinez,

I respectfully ask your permission to use figures 1.2 from your doctoral thesis of 2002, entitled: "Dynamic Subgrid-Scale Modeling for Large-Eddy Simulation of Turbulent Flows with a Stabilized Finite Element Method". I would like to use it in my dissertation entitled: "DNS and LES of Scalar Transfer Across an Air-water Interface during Inception and Growth of Langmuir Circulation".

I really appreciate your help with this.

Best Regards,
Amine Hafsi

C.3 Permissions to Use the Figures in Chapter 4

C.3.1 Permission to Use Figure 4.5b

Copyright Clearance Center **RightsLink®**

Home | Create Account | Help

Taylor & Francis
Taylor & Francis Group

Title: Direct numerical simulation of wind-driven turbulence and scalar transfer at sheared gas–liquid interfaces

Author: Satoru Komori, Ryoichi Kurose, Koji Iwano, et al

Publication: Journal of Turbulence

Publisher: Taylor & Francis

Date: Jan 1, 2010

Rights managed by Taylor & Francis

LOGIN

If you're a copyright.com user, you can login to RightsLink using your copyright.com credentials. Already a RightsLink user or want to learn more?

Thesis/Dissertation Reuse Request

Taylor & Francis is pleased to offer reuses of its content for a thesis or dissertation free of charge contingent on resubmission of permission request if work is published.

BACK | CLOSE WINDOW

C.3.2 Permission to Use Figure 4.7